Plasma Physics and Controlled Fusion

Drift kinetic theory of neoclassical tearing modes in a low collisionality tokamak plasma: magnetic island threshold physics

OPEN ACCESS
IOP Publishing
Plasma Physics and Controlled Fusion
Plasma Phys. Control. Fusion **63** (2021) 054001 (29pp)
https://doi.org/10.1088/1361-6587/abea2e

Drift kinetic theory of neoclassical tearing modes in a low collisionality tokamak plasma: magnetic island threshold physics

A V Dudkovskaia[1,*], J W Connor[2], D Dickinson[1], P Hill[1], K Imada[1], S Leigh[1] and H R Wilson[1]

[1] York Plasma Institute, Department of Physics, University of York, Heslington, York YO10 5DD, United Kingdom
[2] UKAEA-CCFE, Culham Science Centre, Abingdon, Oxon OX14 3DB, United Kingdom

E-mail: avd512@york.ac.uk

Received 15 December 2020, revised 12 February 2021
Accepted for publication 26 February 2021
Published 1 April 2021

Abstract

A new drift kinetic theory for the plasma response to the neoclassical tearing mode (NTM) magnetic perturbation is presented. Small magnetic islands of width, $w \ll a$ (a is the tokamak minor radius) are assumed, retaining the limit $w \sim \rho_{bi}$ (ρ_{bi} is the ion banana orbit width) to include finite orbit width effects. When collisions are small, the ions/electrons follow streamlines in phase space; for passing particles, these lie in surfaces that reproduce the magnetic island structure but have a radial shift by an amount, proportional to $\rho_{\vartheta i/e}$, where $\rho_{\vartheta i/e}$ is the ion/electron poloidal Larmor radius. This shift is associated with the curvature and ∇B drifts and is found to be in opposite directions for $V_{\|} \lessgtr 0$, where $V_{\|}$ is the component of velocity parallel to the magnetic field. The particle distribution function is then found to be flattened across these shifted or *drift* islands rather than the magnetic island. This results in the pressure gradient being sustained across the magnetic island for $w \sim \rho_{\vartheta i}$ and hence reduces the neoclassical drive for NTMs when w is small. This provides a physics basis for the NTM threshold, which is quantified. In Imada *et al* (2019 *Nucl. Fusion* **59** 046016, and references therein), a 4D drift kinetic non-linear code has been applied to describe these modes. In the present paper, the drift island formalism is employed. Valid at low collisionality, it allows a dimensionality reduction to a 3D problem, simplifying the numerical task and efficiently resolving the collisional boundary layer across the trapped-passing boundary. An improved model is adopted for the magnetic drift frequency. This decreases the NTM threshold, compared to the results shown in Imada *et al* (2019 *Nucl. Fusion* **59** 046016, and references therein), making it in quantitative agreement with experimental observations, with $w_c = 0.45\rho_{\vartheta i}$, where w_c is the threshold magnetic island half-width, or $2.85\rho_{bi}$ for the full threshold island width, predicted for our equilibrium.

* Author to whom any correspondence should be addressed.

Keywords: neoclassical tearing mode, tokamak, MHD, NTM threshold, magnetic island, bootstrap current, drift kinetic equation

(Some figures may appear in colour only in the online journal)

1. Introduction

Neoclassical tearing modes (NTM) [1, 2] are classified as large scale resistive magnetohydrodynamic (MHD) plasma instabilities [3]. They limit plasma pressure, reducing fusion gain, and occur in the standard ELMy H-mode, anticipated for the ITER baseline scenario, as well as advanced tokamak scenarios. They can arise in tokamak plasmas due to a filamentation of the plasma current density parallel to the magnetic field lines. This filamentation changes the topology of the magnetic flux surfaces, tearing them apart, to form magnetic islands. Experimentally, NTMs are found to be driven unstable when two criteria are satisfied simultaneously: a threshold in poloidal beta and a threshold island width have to be exceeded. Thus, NTMs are usually triggered above a threshold beta by another MHD perturbation (e.g. sawteeth, fishbones, ELMs, error field locked modes, etc) that creates a primary seed island of sufficient amplitude for NTM growth[3].

According to the conventional theory [1, 2], which requires islands to be sufficiently large, the plasma pressure is quickly equalised around the island due to the large particle and heat transport along magnetic field lines. Thus, in the absence of any heat/particle sources from within the island, the plasma pressure gradient inside the island and hence the total plasma pressure in the core are reduced. This flattening of the pressure profile across the island, in turn, leads to a hole in the bootstrap current near the island O-point, providing the filamentation to drive island growth. As the bootstrap current density rises with beta, the island width also grows with beta, resulting in a degradation of confinement [4–7]. Along with this *soft* beta limit, NTMs with lower poloidal mode numbers can also lead to plasma disruptions through mode locking. There are a number of NTM control techniques [6]; one of them is to generate microwaves at the electron cyclotron frequency to drive current inside the island and replace the missing bootstrap current. This O-point electron cyclotron current drive (ECCD) scheme has demonstrated complete NTM stabilisation on a number of machines and is to be applied to drive the island width down to mitigate the confinement degradation and/or suppress the NTM in fusion devices such as ITER [6]. However, an issue here is to determine how much of the ECCD current is required for the NTM stabilisation and how localised should it be. This leads to a requirement for a more detailed understanding of the threshold physics.

The NTM magnetic islands can either grow or shrink, depending on the filamentary current density perturbation localised to the rational surface, and parallel to the magnetic field, $J_{\|}$. According to the modified Rutherford theory [6–9], the time evolution of the island width is obtained from Ampère's law, which can be expressed in the form:

$$\frac{2\tau_R}{r_s^2}\frac{dw}{dt} = \Delta'(w) + \int J_{\|} d\boldsymbol{q}, \tag{1}$$

where $\tau_R \sim \mu_0 a^2/\eta$ is the resistive diffusion time, η is the local plasma resistivity, w is the island half-width and r_s is the radius of the rational surface, where the safety factor $q(r_s) \equiv q_s = m/n$ with m/n being the poloidal/toroidal mode number of the NTM. Δ' is the classical tearing mode stability parameter [10–13]. It arises due to the free energy in the equilibrium current density, and is calculated from ideal MHD as the discontinuity in the perturbed magnetic flux gradient across the rational surface. In Rutherford's original work [13], only the induced current associated with island growth contributes to $J_{\|}$, and this has been explicitly written through the term on the left hand side of equation (1). Adding tokamak neoclassical effects and particle drift physics, denoted by the second term on the right hand side of equation (1) , leads to the so-called modified Rutherford equation (MRE) [7, 8]. The integral over $\boldsymbol{q}$, where $\boldsymbol{q}$ is a triplet of spatial coordinates, represents an integral across the rational surface of the component of $J_{\|}$ in phase with the magnetic island. The MRE main contributions come from the bootstrap [1, 2], curvature [14, 15] and polarisation [16–18] currents and are denoted by Δ_{bs}, Δ_{cur} and Δ_{pol}, respectively. The perturbed bootstrap current exists in the *banana* collisionality regime in a tokamak and is written through a linear combination of the electron/ion density and temperature gradients. For magnetic islands well above the threshold with no heat/particle sinks/sources, the pressure gradient and the bootstrap current perturbation tends to be removed from within the island, and $\Delta_{bs} \sim \varepsilon^{1/2}(L_q/L_p)(\beta_\vartheta/w)$ [9, 18] and hence is destabilising[4]. Here $\varepsilon = r_s/R_0$ is the inverse aspect ratio with R_0 being the tokamak major radius, β_ϑ is poloidal beta; the safety factor and pressure length scales are $L_{q,p}^{-1} = \pm\nabla_r \ln q, p > 0$ for positive shear. However, the physics is much more complicated for smaller w, relevant for the threshold. According to experimental observations [19, 20], small magnetic islands heal themselves. This fact proves the existence of additional physics to provide the tearing mode threshold. One such threshold mechanism originates from the effects of finite radial diffusion [21, 22, 30] and another arises from finite orbit widths [16, 18, 23–30].

Finite orbit width effects are associated with small magnetic islands of width comparable to the trapped ion banana orbit width, when the polarisation current generally plays a role alongside the bootstrap current. The polarisation current is sensitive to the physics of a layer around the island separatrix.

[3] There is also a special class of the so called *triggerless* NTMs that can grow to the saturated state without any preceding MHD activity.

[4] An exception is for reversed magnetic shear discharges.

The model we discuss below is not particularly rigorous for this. So we restrict consideration to the situation where the equilibrium radial electric field is zero in the island rest frame, in which case the polarisation current is not expected to be important. The dominant physics is then associated with the bootstrap current and curvature.

Δ_{cur} describes the stabilising curvature contribution as an extension of the linear theory, introduced by Glasser, Greene and Johnson [14, 15]. Being an $\mathcal{O}(\varepsilon^2)$ effect, the curvature contribution is generally weak in the large aspect ratio tokamak geometry we consider here. However, in spherical tokamaks the curvature contribution and the bootstrap drive can be comparable [31].

Existing theories of NTMs typically require the island width to be much larger than the ion banana orbit width. There is no analytic theory developed for the neoclassical contributions for $w \lesssim \rho_{bi}$. The MRE form shown in [8] is continued heuristically to a region where $w \sim \rho_{bi}$, but there is no rigorous theoretical justification for it. However, in [32] it has been shown that the marginal island width below which the NTM is removed, i.e. $dw/dt < 0$, is about $2\rho_{bi}$ in both ECCD and beta rampdown discharges and is about $3\rho_{bi}$ in [33]. This is exactly the region where the existing theory breaks down. Thus, a new theory is required to determine all the MRE neoclassical contributions allowing the limit of $w \sim \rho_{bi}$, which is crucial in providing the NTM threshold island width scaling for ITER and other future tokamak devices.

We will consider the low collision frequency limit, $\nu_{ii}/\varepsilon < k_\parallel V_{Ti}$ and $\nu_e/\varepsilon < k_\parallel V_{Te}$, where ν_{ii}/ν_e is the ion/electron collision frequency and $V_{Te/i}$ is the electron/ion thermal velocity. $k_\parallel = k_\vartheta w/L_s$, where $L_s = Rq/s$ is the shear length scale with $s = (r/q)dq/dr$ being the magnetic shear, $k_\vartheta = m/r_s$. We extend our previous results [34–36] to treat the electrons with the same drift kinetic formalism that we use for the ions, while considering magnetic islands at rest in the plasma $\boldsymbol{E}\times\boldsymbol{B}$ frame ($\omega = 0$, where ω is the island propagation frequency in that frame). Earlier work on the ion bootstrap flow considered small islands of $w \sim \rho_{bi}$ by solving the drift kinetic equation through a Monte Carlo computational approach [37, 38]. This simulation confirmed that the ion density gradient is not removed from the region inside small islands. However, [37, 38] focused on the ion response only, omitting the electron response due to the narrowness of the electron banana orbit, and hence neglected the effects of the electrostatic potential that arises from plasma quasi-neutrality. The analytic reduction described here explains the physical origin of the density gradient across the island and provides a new NTM threshold model that arises from both, ion and electron plasma responses. It also provides the self-consistent electrostatic potential, Φ, required to ensure quasi-neutrality. When $w \gg \rho_{\vartheta i}$, the electron and ion distribution functions reproduce the results of the original theory [18] and Φ does not play a major role when the island is at rest in the $\boldsymbol{E}\times\boldsymbol{B}$ reference frame. However, when $\rho_{\vartheta e} \ll w \sim \rho_{\vartheta i}$, we find that the electron and ion solutions differ significantly near the island, highlighting the importance of deriving Φ self-consistently from plasma quasi-neutrality. Once the plasma responses are found, we proceed to the NTM threshold width calculation determining the total perturbed current density along the field lines.

The remainder of the paper is organised as follows. Section 2 introduces the magnetic geometry and the mode dispersion relation. In section 3 we derive the equations describing the plasma response to the NTM magnetic perturbation. The self-consistent electrostatic potential is found in section 4. The drift magnetic island concept is described in section 5. In section 6 we calculate the neoclassical contributions to the MRE and determine the threshold magnetic island width. A conclusion follows. More detailed information, including benchmarking against other models, can be found in appendices A–C.

2. Magnetic topology and NTM dispersion relation

A small inverse aspect ratio, circular poloidal cross section tokamak approximation is considered. A triplet of spatial variables $\{\psi, \varphi, \vartheta\}$ forms an orthogonal set of coordinates[5], satisfying $\boldsymbol{\nabla}\varphi\times\boldsymbol{\nabla}\psi = rB_\vartheta\boldsymbol{\nabla}\vartheta$, where ψ is the poloidal flux function, while φ and ϑ are the toroidal and poloidal angles, respectively; r is the tokamak minor radius and B_ϑ is the poloidal component of the magnetic field. The equilibrium magnetic field is given by:

$$\boldsymbol{B}_0 = I(\psi)\,\boldsymbol{\nabla}\varphi + \boldsymbol{\nabla}\varphi\times\boldsymbol{\nabla}\psi, \tag{2}$$

where $I = RB_\varphi$ depends on the poloidal current, R is the tokamak major radius and B_φ is the toroidal component of the magnetic field. As $\varepsilon \ll 1$ and $B_\vartheta/B_\varphi \sim \varepsilon$, $B_0 = B_\varphi + \mathcal{O}\left(\varepsilon^2 B_\varphi\right)$, where $B_0 = |\boldsymbol{B}_0| \approx B_0(\psi)(1-\varepsilon\cos\vartheta)$. We employ a low beta approximation and to ensure zero divergence of the total magnetic field, we take a magnetic field perturbation associated with the tearing mode to be of the form:

$$\boldsymbol{B}_1 = \boldsymbol{\nabla}\times\left(A_\parallel\boldsymbol{b}_0\right) \tag{3}$$

with $\boldsymbol{b}_0 = \boldsymbol{B}_0/B_0$. $A_\parallel$ is the parallel component of the vector potential connected to the NTM poloidal flux perturbation, $\delta\psi$, via:

$$RA_\parallel = -\delta\psi \tag{4}$$

with $\delta\psi = \tilde{\psi}\cos n\xi$ provided a single isolated NTM island is considered. Here ξ is a helical angle in the island rest frame defined as:

$$\xi = \varphi - q_s\vartheta. \tag{5}$$

$\tilde{\psi} = (w_\psi^2/4)(q_s'/q_s)$ is the NTM perturbation amplitude with w_ψ being the island half-width in ψ space related to w in r space via $w = w_\psi/(RB_\vartheta)$. q_s' denotes $dq/d\psi$ evaluated at the

[5] $\boldsymbol{\nabla}\psi\cdot\boldsymbol{\nabla}\vartheta = \vartheta' R^2 B_\vartheta^2$ with $\vartheta' = \partial\vartheta/\partial\psi|_\chi$ will provide an $\mathcal{O}(\varepsilon^2)$ correction. Here χ is the poloidal variable such that $\boldsymbol{\nabla}\psi\cdot\boldsymbol{\nabla}\chi = 0$ and $\{\psi, \varphi, \chi\}$ forms an orthogonal set of coordinates.

resonant surface, $\psi = \psi_s$. For further analysis, it is convenient to switch from $\{\psi, \varphi, \vartheta\}$ to $\{\psi, \xi, \vartheta\}$. To describe the magnetic island geometry, we introduce a perturbed flux surface function Ω that satisfies $\boldsymbol{B} \cdot \boldsymbol{\nabla}\Omega = 0$:

$$\Omega = \frac{2(\psi - \psi_s)^2}{w_\psi^2} - \cos n\xi, \tag{6}$$

with $\Omega = 1/-1$ corresponding to the separatrix/O-point of the magnetic island, respectively.

To derive the NTM dispersion relation, we address Ampère's law written along the field lines. Projecting out the $J_\parallel$ components that are in and out of phase with the magnetic island and integrating Ampère's law across the island yield:

$$\frac{1}{\mu_0 R}\Delta' \widetilde{\psi} - \int_{\mathbb{R}} d\psi \int_{-\pi}^{\pi} d\xi \bar{J}_\parallel \cos\, n\xi = 0, \tag{7}$$

$$\int_{\mathbb{R}} d\psi \int_{-\pi}^{\pi} d\xi \bar{J}_\parallel \sin\, n\xi = 0. \tag{8}$$

Here we have assumed a stationary magnetic island in the plasma $\boldsymbol{E} \times \boldsymbol{B}$ reference frame to simplify the analysis below[6]. $\bar{J}_\parallel$ is the ϑ-average of $J_\parallel$. Equations (7) and (8) provide a system to be solved for the threshold magnetic island half-width, w_c, and the island propagation frequency, ω, once the perturbed current localised about the island, $J_\parallel$, is obtained. This is to be calculated from the ion and electron distribution functions, which we find in the following sections.

3. Plasma response

The ion/electron response to the NTM magnetic perturbation is described by the drift kinetic equation that reads:

$$\left(V_\parallel \boldsymbol{b} + \boldsymbol{V}_E + \boldsymbol{V}_b\right) \cdot \boldsymbol{\nabla} f_j - \frac{eZ_j}{m_j V}\left[\left(V_\parallel \boldsymbol{b} + \boldsymbol{V}_b\right) \cdot \boldsymbol{\nabla}\Phi\right] \frac{\partial f_j}{\partial V} = C_j f_j \tag{9}$$

in the island rest frame for each particle species, j. A system of two particle species is addressed: plasma electrons and ions. f_j here is to be understood as the gyro-angle independent, leading order distribution function in an expansion in $\rho_{cj}/L \ll 1$, where ρ_{cj} is the Larmor radius of species j and L is the characteristic size of the system. All spatial derivatives in equation (9) are to be calculated at fixed magnetic moment, $\mu = V_\perp^2/2B$, and kinetic energy, $\mathcal{K} = V^2/2$, where V is the particle speed. $(d\mu/dt)\partial f_j/\partial\mu$ is omitted as a higher order correction since $d\mu/dt = \mathcal{O}(\rho_{cj}\beta/L)$[7]. Here $\parallel$ denotes a vector component along the magnetic field lines, $\nabla_\parallel = \boldsymbol{b} \cdot \boldsymbol{\nabla}$, $\boldsymbol{b} = \boldsymbol{B}/B$. $\boldsymbol{V}_E = [\boldsymbol{B} \times \boldsymbol{\nabla}\Phi]/B^2$ and $\boldsymbol{V}_b = -\boldsymbol{V}_\parallel \times \boldsymbol{\nabla}\left(V_\parallel/\omega_{cj}\right)$ are the $\boldsymbol{E} \times \boldsymbol{B}$ and magnetic (∇B and curvature) drift contributions, respectively. $\omega_{cj} = eZ_j B/m_j$ is the cyclotron frequency; eZ_j and m_j are the particle charge and mass. Φ is the electrostatic potential to be determined from the quasi-neutrality requirement. C_j here is a model integro-differential collision operator chosen as in [18] and reproduced in equation (B2).

Expanding about a Maxwell–Boltzmann equilibrium plasma, we write $f_j = f_j^{MB} + g_j$ with $f_j^{MB}(\psi) = n_0(\psi)\pi^{-3/2}V_{Tj}^{-3}(\psi)e^{-V^2/V_{Tj}^2(\psi) - eZ_j\Phi(\psi)/T_j(\psi)}$ being the Maxwell–Boltzmann distribution of a species j. The plasma density, n_{eqm}, is related to n_0 by $n_{eqm} = n_0(1 - eZ_j\Phi/T_j)$, provided $eZ_j\Phi \ll T_j$, where Φ is the electrostatic potential in the island rest frame. $V_{Tj} = (2T_j/m_j)^{1/2}$ is the thermal velocity of a species. g_j describes the perturbation in the particle distribution due to the tearing mode occurrence and also includes the equilibrium neoclassical physics. Seeking a solution localised to the rational surface, we Taylor expand the equilibrium around $\psi = \psi_s$, i.e.

$$f_j = \left(1 - \frac{eZ_j\Phi}{T_j(\psi_s)}\right) f_j^M(\psi_s) + g_j, \tag{10}$$

where $f_j^M(\psi_s) = n_0(\psi_s)\pi^{-3/2}V_{Tj}^{-3}(\psi_s)e^{-V^2/V_{Tj}^2(\psi_s)}$ and $\Phi = \Phi'_{eqm}\big|_{\psi=\psi_s}(\psi - \psi_s) + \delta\Phi$ (prime denotes the derivative with respect to ψ, unless otherwise stated), and thus $\Phi(\psi_s) = \delta\Phi$. Φ_{eqm} is the equilibrium potential in the absence of the island, and $\delta\Phi$ is the perturbation associated with a difference in the electron and ion responses to the magnetic island. For simplicity, below we neglect the equilibrium radial electric field, i.e. $\Phi'_{eqm} = 0$, in the threshold calculation. This is equivalent to considering an island which is at rest in the $\boldsymbol{E} \times \boldsymbol{B}$ rest frame. The perturbed distribution, g_j, then must be linear in ψ far from the island to match to the Maxwellian equilibrium, $\partial g_j/\partial\psi\big|_{\psi\to\pm\infty} = \partial_\psi f_j^M(\psi_s)$, and the electrostatic potential satisfies $\partial\Phi/\partial\psi\big|_{\psi\to\pm\infty} = 0$.

To solve equation (9) for g_j, we define a small parameter $\Delta = w/a \ll 1$ with the following orderings: $eZ_j\Phi/T_j \sim \Delta$, $\delta\Phi/\Phi_{eqm} \sim \Delta$, $B_1 \sim \varepsilon\Delta^2 B_0$ and $g_j/f_j^M \sim \Delta$. Considering equation (27) for electrons and equation (39) for ions from [18], we notice that the dimension of the problem can be reduced by switching from $\{\psi, \xi, \vartheta, \mu, V\}$ to $\{p_\varphi, \xi, \vartheta, \mu, V\}$, where $p_\varphi = \psi - \psi_s - IV_\parallel/\omega_{cj}$ is the toroidal component of the canonical angular momentum. $IV_\parallel/\omega_{cj}$ is the excursion of a particle orbit from the reference flux surface. As $w \ll a$, the plasma is toroidally symmetric to leading order and thus we expect the toroidal component of p_φ to be approximately constant on a particle orbit. To rigorously demonstrate this, we employ an expansion in Δ and write $g_j = \sum_\alpha g_j^{(\alpha)}\Delta^\alpha$. To $\mathcal{O}(\Delta^0)$, we have $\partial g_j^{(0)}/\partial\vartheta\Big|_{p_\varphi,\xi} = 0$ and hence we learn that the leading order distribution function, $g_j^{(0)}$, is independent of ϑ at fixed p_φ, i.e. $g_j^{(0)}(\psi, \xi, \vartheta, \mu, V) = g_j^{(0)}(p_\varphi, \xi, \mu, V)$. As we consider the banana collisionality regime, the collision operator on the right hand side of equation (9) has been assumed to be order Δ smaller than the free streaming.

[6] In its general form, equation (7) is to be replaced with equation (1).

[7] Terms proportional to $\partial/\partial t$ in $d\mu/dt$ do not contribute in the island rest frame, and $\rho_{cj}\boldsymbol{b} \cdot \boldsymbol{\nabla} \times \boldsymbol{b} \sim \rho_{cj}\beta/L$.

Proceeding to next order in Δ, we obtain in a low beta limit:

$$\frac{1}{q}\frac{\partial g_j^{(1)}}{\partial\vartheta}\bigg|_{p_\varphi,\xi,\mu,V} + \left[\frac{R^2}{I}(\boldsymbol{B}_1\cdot\boldsymbol{\nabla}p_\varphi) + \frac{R^2B_0}{IV_\parallel}\frac{\partial\Phi}{\partial\xi}\bigg|_{\psi,\vartheta}\right]\frac{\partial g_j^{(0)}}{\partial p_\varphi}\bigg|_{\xi,\vartheta,\mu,V} + \left[\frac{q_s'}{q}\left(p_\varphi+\frac{IV_\parallel}{\omega_{cj}}\right) + \frac{R^2B_0^2}{I}\frac{\partial}{\partial\psi}\bigg|_{\vartheta,\xi}\left(\frac{V_\parallel}{\omega_{cj}}\right) + \frac{R^2B_\vartheta^2}{I}\vartheta'\frac{\partial}{\partial\vartheta}\bigg|_{\psi,\xi}\left(\frac{V_\parallel}{\omega_{cj}}\right) - \frac{R^2B_0}{IV_\parallel}\frac{\partial\Phi}{\partial\psi}\bigg|_{\xi,\vartheta}\right]\frac{\partial g_j^{(0)}}{\partial\xi}\bigg|_{p_\varphi,\vartheta,\mu,V} - \frac{eZ_j}{m_jqV}\frac{\partial\Phi}{\partial\vartheta}\bigg|_{p_\varphi,\xi}\frac{\partial g_j^{(0)}}{\partial V}\bigg|_{p_\varphi,\xi,\vartheta,\mu} = \frac{R^2B_0}{IV_\parallel}C_jg_j^{(0)}. \tag{11}$$

$\boldsymbol{B}_1\cdot\boldsymbol{\nabla}\vartheta$ and $\boldsymbol{B}_1\cdot\boldsymbol{\nabla}\xi$ have been neglected as higher order terms in the limit of small magnetic islands[8]. We note that $\partial/\partial\psi,\ \partial/\partial p_\varphi\sim 1/RB_\vartheta r$ when acting on equilibrium quantities and $\partial/\partial\psi,\ \partial/\partial p_\varphi\sim 1/RB_\vartheta w$ on perturbed quantities ($\partial p_\varphi/\partial\psi=1$ to leading order in $\rho_{\vartheta j}/a$). To solve equation (11) for $g_j^{(0)}$, we have to eliminate the term in $g_j^{(1)}$, integrating the equation over ϑ at fixed p_φ. This is equivalent to an orbit-averaging procedure. For passing particles, g_j is periodic in ϑ and thus we simply integrate over a period in ϑ, assuming $g_j(-\pi)=g_j(\pi)$. Trapped particles oscillate between bounce points, $\pm\vartheta_b$, defined from $\lambda B_0(\vartheta_b)=1$, where $V_\parallel$ tends to zero. Thus, for them we integrate between $\pm\vartheta_b$ and sum over σ, where $\sigma=V_\parallel/|V_\parallel|$ and $\lambda=2\mu/V^2$ is the pitch angle. As continuity is required at each bounce point, this annihilates the $\partial g_j^{(1)}/\partial\vartheta\big|_{p_\varphi}$ term.

To employ the collision operator from [18], we switch from $\{\mu,V\}$ to $\{\lambda,V;\sigma\}$ in velocity space. Thus, the velocity space integral and $V_\parallel$ become:

$$\int d\boldsymbol{V} = \pi B\sum_\sigma\int_{\mathbb{R}^+}V^2dV\int_0^{B^{-1}}\frac{d\lambda}{(1-\lambda B)^{1/2}}, \tag{12}$$

$$V_\parallel = \sigma V(1-\lambda B)^{1/2}. \tag{13}$$

The trapped-passing boundary in pitch angle space is then located at the inverse of the maximum value of the magnetic field, i.e. $\lambda_c=1/B_0(1+\varepsilon)$ for the equilibrium given above. $\lambda\in[0,\lambda_c]$ for passing and $\lambda\in(\lambda_c,\lambda_{fin}]$ with $\lambda_{fin}=1/B_0(1-\varepsilon)$ for trapped particles. Therefore, an orbit-averaged form of equation (11) reads:

$$\left[\frac{q_s'}{q}p_\varphi\cdot\Theta(\lambda_c-\lambda)+\omega_D-\omega_{E,\xi}\right]\frac{\partial g_j^{(0)}}{\partial\xi}\bigg|_{p_\varphi,\lambda,V} + \left[\left\langle\frac{R^2}{I}(\boldsymbol{B}_1\cdot\boldsymbol{\nabla}p_\varphi)\right\rangle_\vartheta^{p_\varphi}+\omega_{E,r}\right]\frac{\partial g_j^{(0)}}{\partial p_\varphi}\bigg|_{\xi,\lambda,V} = \left\langle\frac{R^2B_0}{IV_\parallel}C_j\right\rangle_\vartheta^{p_\varphi}g_j^{(0)}, \tag{14}$$

where

$$\omega_D = \frac{q_s'}{q}\left\langle\frac{IV_\parallel}{\omega_{cj}}\right\rangle_\vartheta^{p_\varphi} + \frac{1}{I}\left\langle R^2B_0^2\frac{\partial}{\partial\psi}\bigg|_{\xi,\vartheta}\left(\frac{V_\parallel}{\omega_{cj}}\right)\right\rangle_\vartheta^{p_\varphi},$$
$$\omega_{E,\xi} = \frac{1}{I}\left\langle\frac{R^2B_0}{V_\parallel}\frac{\partial\Phi}{\partial\psi}\bigg|_{\xi,\vartheta}\right\rangle_\vartheta^{p_\varphi},\quad \omega_{E,r} = \frac{1}{I}\left\langle\frac{R^2B_0}{V_\parallel}\frac{\partial\Phi}{\partial\xi}\bigg|_{\psi,\vartheta}\right\rangle_\vartheta^{p_\varphi} \tag{15}$$

are the magnetic and $\boldsymbol{E}\times\boldsymbol{B}$ drift frequencies in ξ and radial directions, respectively, to $\mathcal{O}(\varepsilon\Delta g_j)$[9]. Θ denotes the Heaviside step function. The ϑ-averaging operator at fixed p_φ is defined as:

$$\langle\ldots\rangle_\vartheta^{p_\varphi} = \begin{cases}\frac{1}{2\pi}\int_{-\pi}^{\pi}\ldots d\vartheta, & \lambda\le\lambda_c\\ \frac{1}{4\pi}\sum_\sigma\sigma\int_{-\vartheta_b}^{\vartheta_b}\ldots d\vartheta, & \lambda\ge\lambda_c.\end{cases} \tag{16}$$

Φ has been assumed to be periodic in ϑ. Using equation (3), we find $\langle R^2(\boldsymbol{B}_1\cdot\boldsymbol{\nabla}p_\varphi)\rangle_\vartheta^{p_\varphi}\partial g_j^{(0)}/\partial p_\varphi = -\langle R^2B_0dA_\parallel/d\xi\rangle_\vartheta^{p_\varphi}\partial g_j^{(0)}/\partial p_\varphi+\mathcal{O}(\Delta^2g_jRB_0)$ taking $\boldsymbol{\nabla}p_\varphi=\boldsymbol{\nabla}\psi$ to leading order in $\rho_{\vartheta j}/a$. Due to equation (4), $dA_\parallel/d\xi=(\widetilde{\psi}/R)\sin\xi$ for a 2/1 single isolated magnetic island and thus $\langle R^2(\boldsymbol{B}_1\cdot\boldsymbol{\nabla}p_\varphi)/I\rangle_\vartheta^{p_\varphi}=-w_\psi^2q_s'B_0/(4q_sB_\varphi)\sin\xi\cdot\Theta(\lambda_c-\lambda)$. Equation (14) is the final orbit-averaged non-normalised equation for the ion/electron response to $\mathcal{O}(\Delta^1)$ in $\{p_\varphi,\xi,\lambda,V;\sigma\}$ space. Following [18], we close our system by taking a collision operator that conserves particles and momentum, i.e. C_j is given by equation (62) of [18] and retains like-particle and electron-ion collisions.

4. Plasma quasi-neutrality and electrostatic potential

We adopt a Maxwell–Boltzmann equilibrium and so we obtain:

$$\hat{n}_{i/e} = 1\mp\delta\hat{\Phi}+\delta\hat{n}_{i/e} \tag{17}$$

for the ion/electron density integrating equation (10) over velocity space. Here $\hat{n}_j=n_j/n_0$, $\delta\hat{n}_j=\delta n_j/n_0$ and $\delta\hat{\Phi}=e\delta\Phi/T_j$ provided $Z_i=1$ and $T_e=T_i$ (this assumption

[8] A detailed derivation can be found in [39].

[9] See appendix A for more detail.

is maintained throughout the paper unless otherwise stated). δn_j is the perturbed density associated with g_j. Thus, balancing the electron and ion densities, we find:

$$\delta\hat{\Phi} = \frac{\delta\hat{n}_i - \delta\hat{n}_e}{2} \tag{18}$$

for the perturbed potential. We adopt an iteration process such that at each iteration step, k, we solve $\delta\hat{\Phi}^{(k+1)} = (1/2)\left(\delta\hat{n}_i^{(k)} - \delta\hat{n}_e^{(k)}\right)$, where $\delta\hat{n}_{i,e}^{(k)} = \delta\hat{n}_{i,e}^{(k)}(\delta\hat{\Phi}^{(k)})$ are ion and electron densities for $\delta\hat{\Phi} = \delta\hat{\Phi}^{(k)}$. The iteration proceeds until $\delta\hat{\Phi}^{(k+1)} = \delta\hat{\Phi}^{(k)}$ to some defined accuracy. Thus, in contrast to [37], we allow the restoration of the density/temperature gradient across the magnetic island to be influenced by both ions and electrons.

5. Reduced drift kinetic formulation for low collision frequency

5.1. Drift islands

To analyse equation (14) further, we introduce the following dimensionless system:

$$\hat{\rho}_{\vartheta j} = \frac{IV_{Tj}}{\omega_{cj} w_\psi}, \quad x = \frac{\psi - \psi_s}{w_\psi}, \quad \hat{V}_{\|j} = \frac{V_\|}{V_{Tj}}, \quad \hat{V}_j = \frac{V}{V_{Tj}},$$
$$\hat{L}_q^{-1} = \frac{q_s'}{q}\psi_s, \quad \hat{L}_B^{-1} = \frac{\psi_s}{B}\frac{\partial B}{\partial \psi}, \quad \hat{w} = \frac{w_\psi}{\psi_s}, \quad \hat{\psi} = \frac{\psi}{w_\psi}$$
$$\hat{\Phi} = \frac{e\Phi}{T_j(\psi_s)}, \quad \hat{p}_\varphi = x - \hat{\rho}_{\vartheta j}\hat{V}_\| \tag{19}$$

(note: λ is kept non-normalised and we adopt the convention $\psi = 0$ at the magnetic axis). Employing the large aspect ratio, circular cross section tokamak approximation, assuming that the fastest radial variation is in perturbed quantities and taking $\partial\hat{p}_\varphi/\partial\hat{\psi} = 1$ to leading order in $\rho_{\vartheta j}/a$, we derive:

$$\left[\frac{\hat{w}}{\hat{L}_q}\hat{p}_\varphi \cdot \Theta(\lambda_c - \lambda) - \hat{\rho}_{\vartheta j}\hat{\omega}_D - \right.$$
$$\left. - \frac{\partial}{\partial \hat{p}_\varphi}\bigg|_{\xi,\vartheta} \frac{1}{2}\left\langle \frac{\hat{\rho}_{\vartheta j}}{\hat{V}_\|}\hat{\Phi}\right\rangle_\vartheta^{p_\varphi}\right] \frac{\partial g_j^{(0)}}{\partial \xi}\bigg|_{S,\lambda,V} = \hat{C}_j g_j^{(0)}, \tag{20}$$

from equation (14), where the stream function, S, is

$$S = \frac{\hat{w}}{4\hat{L}_q}\left[2\left(\hat{p}_\varphi - \frac{\hat{\omega}_D\hat{\rho}_{\vartheta j}\hat{L}_q}{\hat{w}}\right)^2 - \cos\xi\right]\Theta(\lambda_c - \lambda) -$$
$$- \hat{\omega}_D\hat{\rho}_{\vartheta j}\hat{p}_\varphi\Theta(\lambda - \lambda_c) - \frac{1}{2}\left\langle\frac{\rho_{\vartheta j}}{\hat{V}_\|}\hat{\Phi}\right\rangle_\vartheta^{p_\varphi}. \tag{21}$$

Here $\hat{\omega}_D$ and $\hat{C}_j g_j^{(0)}$ denote the normalised forms of ω_D and the right hand side of equation (14) [39]. Their explicit representations can be found in appendix B, where we show that $\hat{C}_j$ contains the pitch angle scattering and diffusion in S space. S is to be treated as a new *radial* coordinate. We note that, in contrast to ψ or p_φ, S has a different representation for passing and trapped particles; this will provide a complication for matching at the trapped-passing boundary, $\lambda = \lambda_c$.

Equations (20) and (21) complete the transformation from $\{p_\varphi, \xi, \lambda, V; \sigma\}$ to $\{S, \xi, \lambda, V; \sigma\}$, and the particle distribution function is now to be found as $g_j^{(0)} = g_j^{(0)}(S, \xi, \lambda, V; \sigma)$. According to its definition, S is a function of p_φ, ξ, λ and V for each σ, and depends on the form of the electrostatic potential, which is, in turn, a function of ψ, ξ and ϑ. For passing particles in the absence of the electrostatic potential, i.e. when the $\boldsymbol{E}\times\boldsymbol{B}$ drift effects are ignored, the contours of constant S reproduce the magnetic island structure given by the constant Ω contours (see equation (6)) but have a radial shift by the amount $\hat{\omega}_D\hat{\rho}_{\vartheta j}\hat{L}_q/\hat{w} + \hat{\rho}_{\vartheta j}\hat{V}_\|$, which is proportional to the poloidal Larmor radius. This shift arises from ∇B and curvature tokamak drifts, and as $\hat{\omega}_D$ is σ-dependent in the passing branch, the shift is in opposite directions for $V_\| \gtrless 0$. We refer to these island structures in the contours of constant S as *drift* islands. Inclusion of Φ, in principle, might modify the structure of constant S contours. However, the electrostatic potential calculated iteratively to ensure plasma quasi-neutrality does not add any significant qualitative modifications to the form of S; specifically, the surfaces of constant S in the (x, ξ) plane are island-like for passing and open for trapped particles even with Φ included. Examples for passing particles are shown in figure 1 for (a) $\rho_{\vartheta i}/w = 0.05 \ll 1$ and (b) $\rho_{\vartheta i}/w = 0.4$. A similar drift island structure in view of plasma tokamak transport has been identified by Kadomtsev in [40], where the chains of islands much smaller than $\rho_{\vartheta i}$ but larger than $\rho_{\vartheta e}$ are considered.

To solve equation (20) for $g_j^{(0)}$ as a function of S, we employ weak collisional dissipation. In the reference frame in which the equilibrium radial electric field is zero, this is equivalent to imposing $\delta_i \equiv \nu_{ii}/\varepsilon k_\| V_{Ti} \ll 1$ for ions and $\delta_e \equiv \nu_e/\varepsilon k_\| V_{Te} \ll 1$ for electrons. Employing the perturbation theory again, and applying an expansion in δ_j, we obtain $\partial g_j^{(0,0)}/\partial\xi\big|_{S,\vartheta} = 0$ to leading order. From this we learn that $g_j^{(0,0)}$ is independent of ξ at fixed S, i.e. $g_j^{(0,0)}(p_\varphi, \xi, \lambda, V; \sigma) = g_j^{(0,0)}(S, \lambda, V; \sigma)$. Thus, we find that the particle distribution function is constant along these S streamlines in the absence of collisions. Proceeding to next order in δ_j and introducing collisions, we derive:

$$\mathcal{A}\frac{\partial g_j^{(0,1)}}{\partial\xi}\bigg|_{S,\vartheta,\lambda,V} = \hat{C}_j g_j^{(0,0)}, \tag{22}$$

where $\mathcal{A}$ denotes the coefficient in front of $\partial g_j^{(0)}/\partial\xi\big|_{S,\vartheta,\lambda,V}$ on the left hand side of equation (20). Equation (22) allows us to reconstruct the actual form of the ion/electron distribution, i.e. its S and λ dependence. To eliminate the term in $g_j^{(0,1)}$, we divide both sides of equation (22) by $\mathcal{A}$ and introduce the annihilation operator similar to equation (16) to provide ξ-averaging at fixed S. For open contours (i.e. for passing particles outside the drift island and for trapped particles), we integrate equation (22) over a period in ξ, imposing periodicity at $\xi = \pm\pi$. For closed contours, i.e. passing particles inside the drift island, we integrate between the ξ-bounce points given by

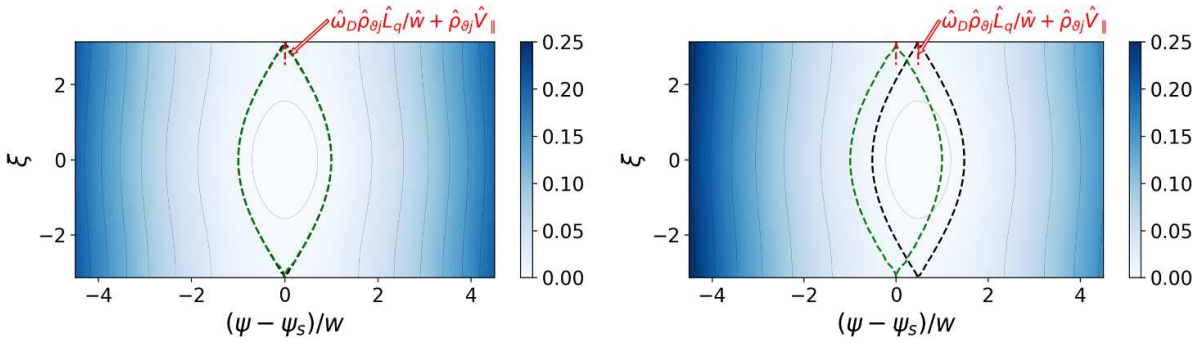

(a) $w \gg \rho_{\vartheta i}$, $w = 0.02 r_s$, $\rho_{\vartheta i} = 1.0 \cdot 10^{-3} r_s$ (b) $w \gtrsim \rho_{\vartheta i}$, $w = 0.02 r_s$, $\rho_{\vartheta i} = 8.0 \cdot 10^{-3} r_s$

Figure 1. Contours of constant S in the (x, ξ) plane in the absence of the electrostatic potential, $\hat{\Phi} = 0$, for (a) $w/\rho_{\vartheta i} = 20$ and (b) $w/\rho_{\vartheta i} = 2.5$. Parameters are $\lambda/\lambda_c = 0.92$, $\varepsilon = 0.1$, $V = V_{Ti}$, $\sigma = +1$, $\hat{L}_q = 1$. Green dashed line indicates the position of the magnetic island separatrix, $\Omega = 1$. The S island separatrix is at $S = S_c = \hat{w}/4\hat{L}_q$ (black dashed line).

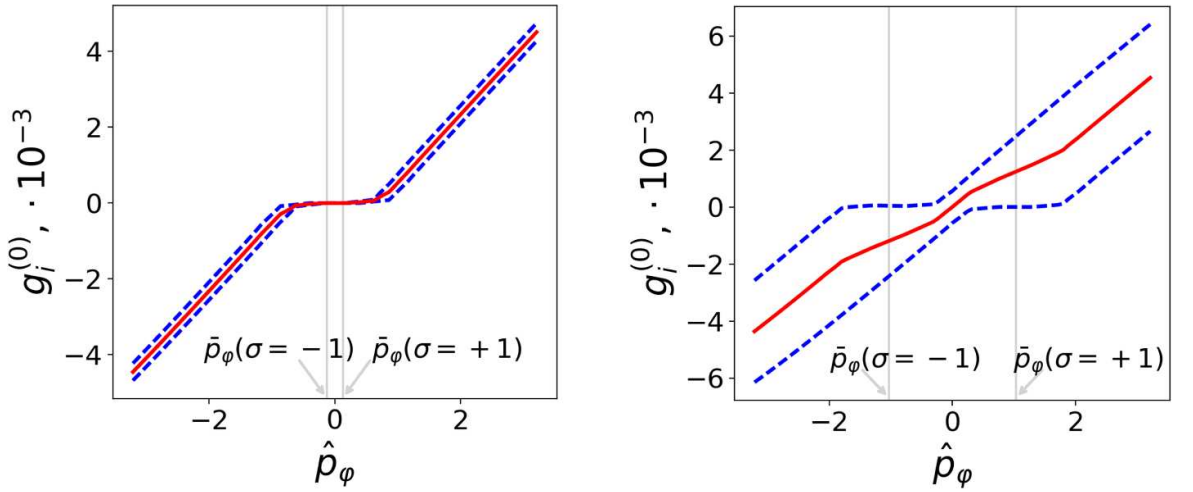

(a) $w \gg \rho_{\vartheta i}$, $w = 0.02 r_s$, $\rho_{\vartheta i} = 1.0 \cdot 10^{-3} r_s$ (b) $w \gtrsim \rho_{\vartheta i}$, $w = 0.02 r_s$, $\rho_{\vartheta i} = 8.0 \cdot 10^{-3} r_s$

Figure 2. Sketch of the ion distribution function vs. $\hat{p}_\varphi$ at $\lambda/\lambda_c = 0.98$, $\xi = 0$ for (a) $w/\rho_{\vartheta i} = 20$ and (b) $w/\rho_{\vartheta i} = 2.5$. $g_i^{(0)}$ is normalised to $n_{eqm}/(\pi^{3/2} V_{Ti}^3)$. $\varepsilon = 0.1$, $\hat{L}_q = 1$. Ion density/temperature length scales, $L_n/L_{Ti} = 1$. $\bar{p}_\varphi(\sigma) = \hat{\omega}_D(\sigma)\hat{\rho}_{\vartheta i}\hat{L}_q/\hat{w}$. Dashed lines indicate the $\sigma = \pm 1$ passing ion distribution function, $g_i^{(0),\sigma}$, while solid line represents $\frac{1}{2}\sum_\sigma g_i^{(0),\sigma}$. The $\sigma = \pm 1$ drift islands are centred around $\bar{p}_\varphi(\sigma = \pm 1)$, denoted by grey vertical lines. The magnetic island is located between them; $\hat{p}_\varphi = \pm 1$ corresponds to the separatrix of the magnetic island.

$\xi_{b1,2} = \xi_{b1,2}(S, p_{\varphi 0}, \lambda, V; \sigma)$, where $p_{\varphi 0}$ is the stationary point of $S = S(p_\varphi)$ for each ξ, λ, V and σ, and also sum over the two sides of the closed contours, $\sigma_{p_\varphi} = \pm 1$, where σ_{p_φ} is the sign of $p_\varphi - p_{\varphi 0}$. Continuity at each ξ-bounce point then eliminates $g_j^{(0,1)}$. Thus, equation (22) reduces to:

$$\left\langle \frac{\hat{C}_j}{\mathcal{A}} \right\rangle_\xi^S g_j^{(0,0)} = 0 \tag{23}$$

with the ξ-averaging operator at fixed S being defined as:

$$\langle \ldots \rangle_\xi^S = \begin{cases} \frac{1}{2\pi} \int_{-\pi}^{\pi} \ldots d\xi, & S \geq S_c \\ \frac{1}{4\pi} \sum_{\sigma_{p_\varphi}} \sigma_{p_\varphi} \int_{\xi_{b,1}}^{\xi_{b,2}} \ldots d\xi, & S < S_c \end{cases} \tag{24}$$

for passing (S_c denotes the drift island separatrix and is to be updated at the end of each iteration in Φ for passing particles) and:

$$\langle \ldots \rangle_\xi^S = \frac{1}{2\pi} \int_{-\pi}^{\pi} \ldots d\xi \tag{25}$$

for trapped particles. The explicit form of the $\left\langle \hat{C}_j/\mathcal{A} \right\rangle_\xi^S$ operator is discussed in appendix B. From the S island formalism we learn that while collisions are neglected in equation (20), the combined effect of the parallel streaming, ∇B and curvature drifts would force the passing particle distribution to be flattened inside these drift islands rather than the actual magnetic island. Introducing collisions at next order fully determines the perturbed distribution function via equation (23) and the results of appendix B. This provides a physics basis for the NTM threshold by reducing the neoclassical drive for NTMs of width $w \sim \rho_{\vartheta i}$ when the radial shift in the contours of constant S, compared to Ω, is significant.

A schematic ion distribution function vs. $\hat{p}_\varphi$ is shown in figures 2(a) and (b) at small and large $\rho_{\vartheta i}/w$. At small $\rho_{\vartheta i}/w$ and hence small radial shift in S, equation (21), a sum of the ion distribution functions over $\sigma = \pm 1$ is found to be flattened inside the magnetic island in the vicinity of $\hat{p}_\varphi = 0$. From equation (12), this would result in flattening of the ion density profile around the magnetic island O-point for $\rho_{\vartheta i}/w \ll 1$. In contrast, when the radial shift of the drift islands compared to the magnetic island becomes significant, the flattening of $\sum_\sigma g_i^{(0),\sigma}$ and hence the density flattening are removed from inside the magnetic island, e.g. $\rho_{\vartheta i} = 7.0 \times 10^{-3} r_s$ is sufficient to partially restore the density gradient across the magnetic island of width $w = 0.02 r_s$. If $\rho_{\vartheta i}/w \gtrsim 1$, the profile will be further steepened across the O-point. This results in the density gradient being restored in the vicinity of the island O-point. The corresponding density profiles are shown in figure 3. We highlight that the gradient inside the magnetic island is a consequence of the drift island structures, and thus is a property of the passing (and not trapped) particles.

For electrons, the radial shift in equation (21) is small as $\rho_{\vartheta e} \ll \rho_{\vartheta i}$. Hence, the drift island effect is less significant for the electron distribution function. This creates a significant difference in the electron and ion density profiles especially at large $\rho_{\vartheta i}$ in the absence of the electrostatic potential. Indeed, when $\rho_{\vartheta i}/w \ll 1$, the ion and electron density gradients are both removed from inside the magnetic island due to strong parallel streaming along perturbed flux surfaces, so there the role of Φ is not crucial. In contrast, when $\rho_{\vartheta i}$ and w are comparable, a non-zero, finite ion density gradient is sustained around the magnetic island O-point, while the electron density gradient is still removed in the absence of any potential due to the strong electron parallel streaming and $\rho_{\vartheta e} \ll w$. However, to maintain plasma quasi-neutrality, the electrostatic potential is required, which adjusts to provide $n_i \approx n_e$. Hence, the ion density steepening at large $\rho_{\vartheta i}$ is explained by the radial shift in S given by equation (21), while the sustainability of the electron density gradient is associated with the self-consistent electrostatic potential.

The particle flow along the field lines is $u_{\|j} = n_0^{-1} \int g_j V_\| d\boldsymbol{V}$, and thus $\sum_\sigma \sigma g_i^{(0),\sigma}$ represents the parallel flow moment due to equations (12) and (13). The main contribution to the flow is provided by passing particles due to the summation over σ in the ϑ-averaging operator introduced for trapped particles, equation (16). However, the trapped branch also contributes as the integration here is imposed at fixed ψ, and the trapped particle distribution function is $g_i^{(0)}(\hat{p}_\varphi, \xi, \lambda, \hat{V}) = g_i^{(0)}(\hat{\psi}, \xi, \vartheta, \lambda, \hat{V}; \sigma)$ with $\hat{p}_\varphi = x - \hat{\rho}_{\vartheta i} \hat{V}_\| = x - \sigma \hat{\rho}_{\vartheta i} \hat{V} \sqrt{1 - \lambda B(\vartheta)}$.

In figure 4 we show contours of the parallel component of the ion flow, $u_{\|i}$, at different $\rho_{\vartheta i}/w$ in the (ψ, ξ) plane. In figure 4(a) for the smallest $\rho_{\vartheta i}/w = 0.05$, $u_{\|i}$ is flattened and zero across the magnetic island O-point in accordance with the conventional picture when the neoclassical flow experiences a hole around the island O-point. In figures 4(b)–(d), corresponding to larger $\rho_{\vartheta i}/w$, there is a non-zero contribution

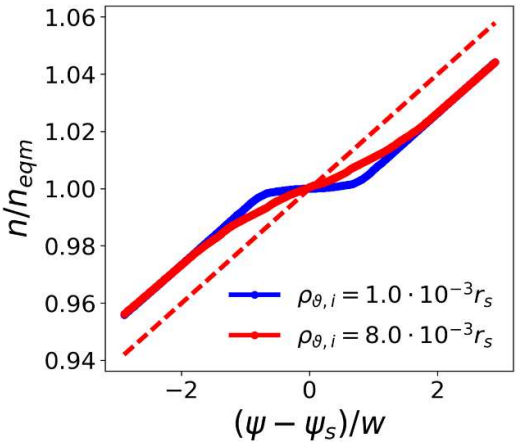

Figure 3. Radial density profile across the magnetic island O-point ($\xi = 0$) for different $\rho_{\vartheta i}$. $w = 0.02 r_s$, $\varepsilon = 0.1$, $\hat{L}_q = 1$, ion collisionality $\nu_i^* = 10^{-4}$. Dashed line indicates the axisymmetric equilibrium density profile, $\propto L_n^{-1} \hat{w} \hat{\psi}$, $\Phi'_{eqm} = 0$. Here n_{eqm} is the equilibrium density, i.e. in the absence of the magnetic island.

to $\sum_\sigma \sigma g_i^{(0),\sigma}$ inside the island and thus there is some flow that penetrates into the island. This contribution grows with growing $\rho_{\vartheta i}/w$ and spreads further into the island, which provides the basis for an NTM threshold. The corresponding ϑ-averaged parallel component of the current density that contributes to equation (7) is shown in figure 5 for small and large $\rho_{\vartheta i}/w$. The corresponding electrostatic potential is shown in figure 6.

5.2. Dissipation layer in the vicinity of the trapped-passing boundary

The perturbative approach we applied above in section 5 to eliminate the ξ-dependence at fixed S breaks down in a *dissipation* layer, i.e. a narrow region in pitch angle in the vicinity of the trapped-passing boundary, $\lambda = \lambda_c$ (see figure 7). Here collisional dissipation becomes comparable to parallel streaming, $\nu_{ii/e} \partial^2/\partial \lambda^2 \sim \mathcal{A} \partial/\partial \xi|_S$, due to a steep gradient in λ, and thus a full solution of equations (14)/(20) is required in the layer, close to $\lambda = \lambda_c$. This steep gradient region arises because the different orbit-averaging procedures for passing and trapped particles produce a discontinuity at $\lambda = \lambda_c$, and the layer resolves this discontinuity.

Following [18], we impose the matching conditions given by equations (106)–(108) of [18] at the trapped-passing boundary to provide continuity of the particle distribution function and its first λ derivative across the boundary. We note that originally matching is imposed at fixed ψ. However, switching from ψ to S and solving equation (23) at the 0th iteration in Φ, we find $g_j^{(0,0)} = g_j^{(0,0)}(S, \lambda, V; \sigma) = g_j^{(0,0)}[S(p_\varphi, \xi, \lambda, V; \sigma), \lambda, V; \sigma]$ for the leading order passing and $g_j^{(0,0)} = g_j^{(0,0)}(S, \lambda, V; \sigma) = g_j^{(0,0)}[S(p_\varphi, \lambda, V; \sigma), \lambda, V; \sigma]$ for the leading order trapped particle distribution. The different forms for S in the passing/trapped regions do not allow continuity of the particle distribution across the trapped-passing boundary at fixed

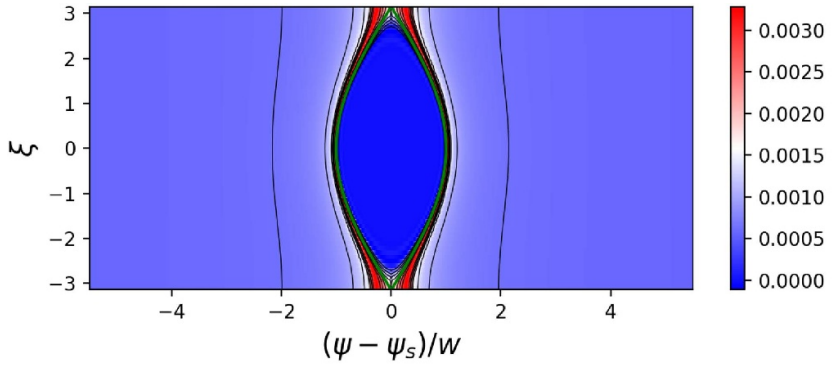

(a) $w = 0.02r_s,\ \rho_{\vartheta i} = 1.0 \cdot 10^{-3} r_s$

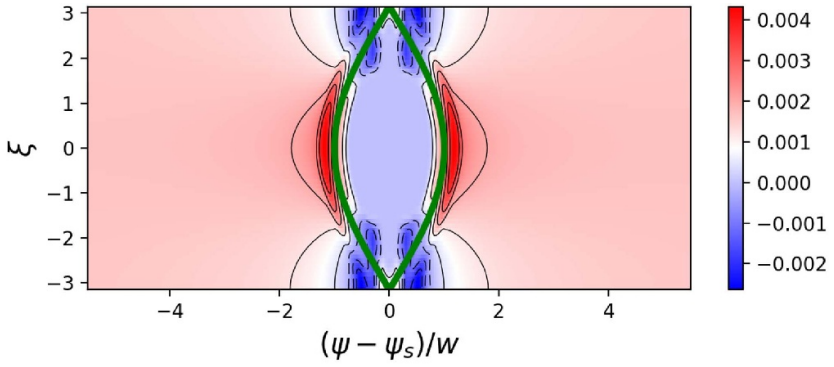

(b) $w = 0.02r_s,\ \rho_{\vartheta i} = 7.0 \cdot 10^{-3} r_s$

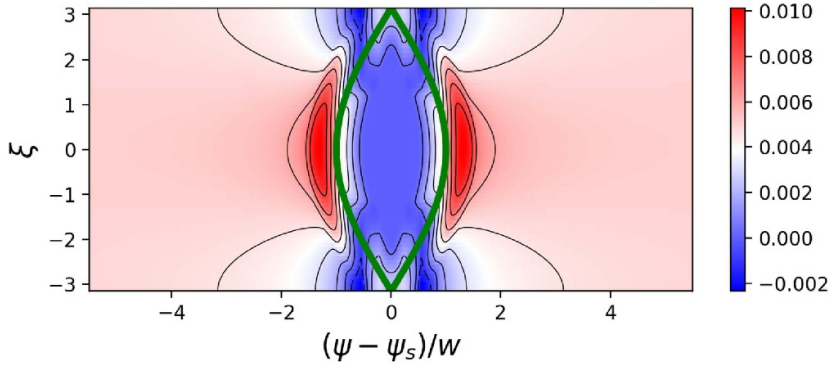

(c) $w = 0.02r_s,\ \rho_{\vartheta i} = 1.2 \cdot 10^{-2} r_s$

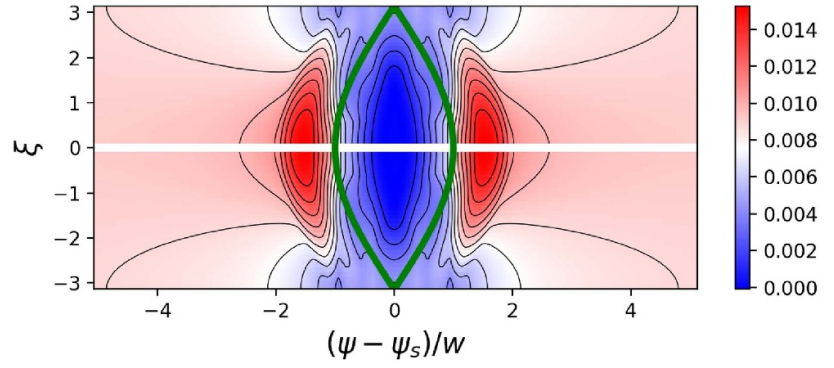

(d) $w = 0.02r_s,\ \rho_{\vartheta i} = 2.0 \cdot 10^{-2} r_s$

Figure 4. Colour contours showing the ion parallel flow, $u_{\|i}$, as a function of x and ξ plotted at different $\rho_{\vartheta i}/w$. $u_{\|i}$ is normalised to V_{Ti}. $\varepsilon = 0.1$, $\hat{L}_q = 1$, $L_B^{-1} = 0$, $L_n/L_{Ti} = 1$, $\nu_i^* = 10^{-3}$. The green line indicates the position of the magnetic island separatrix, $\Omega = 1$.

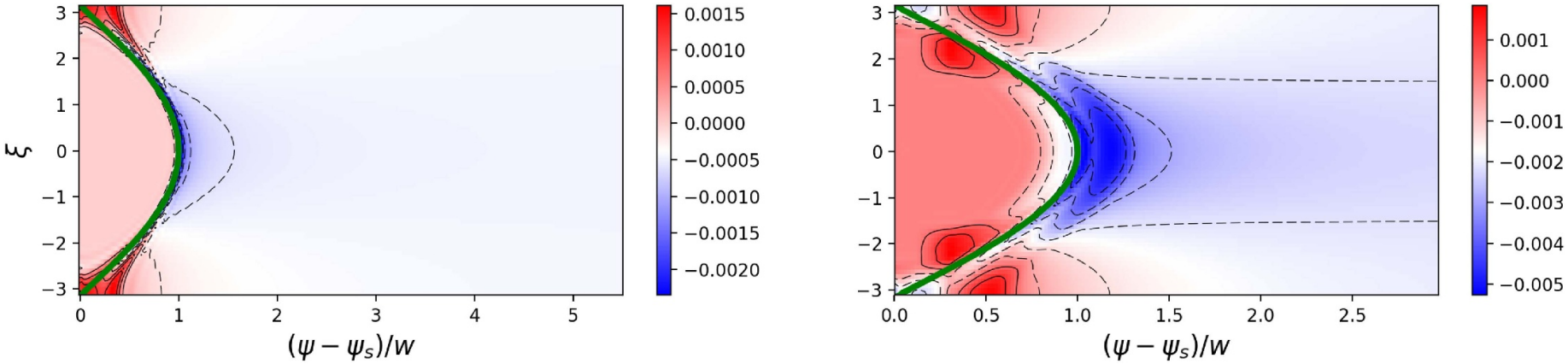

Figure 5. Colour contours showing the parallel current density, $J_\parallel$, averaged over ϑ for $\rho_{\vartheta i}/w = 0.05$ (left) and $\rho_{\vartheta i}/w = 0.35$ (right). $J_\parallel$ is normalised to eV_{Ti}. $\varepsilon = 0.1$, $\hat{L}_q = 1$, $L_B^{-1} = 0$, $L_n/L_{Ti} = 1$, $\nu_i^* = 10^{-3}$. The green line indicates the position of the magnetic island separatrix, $\Omega = 1$.

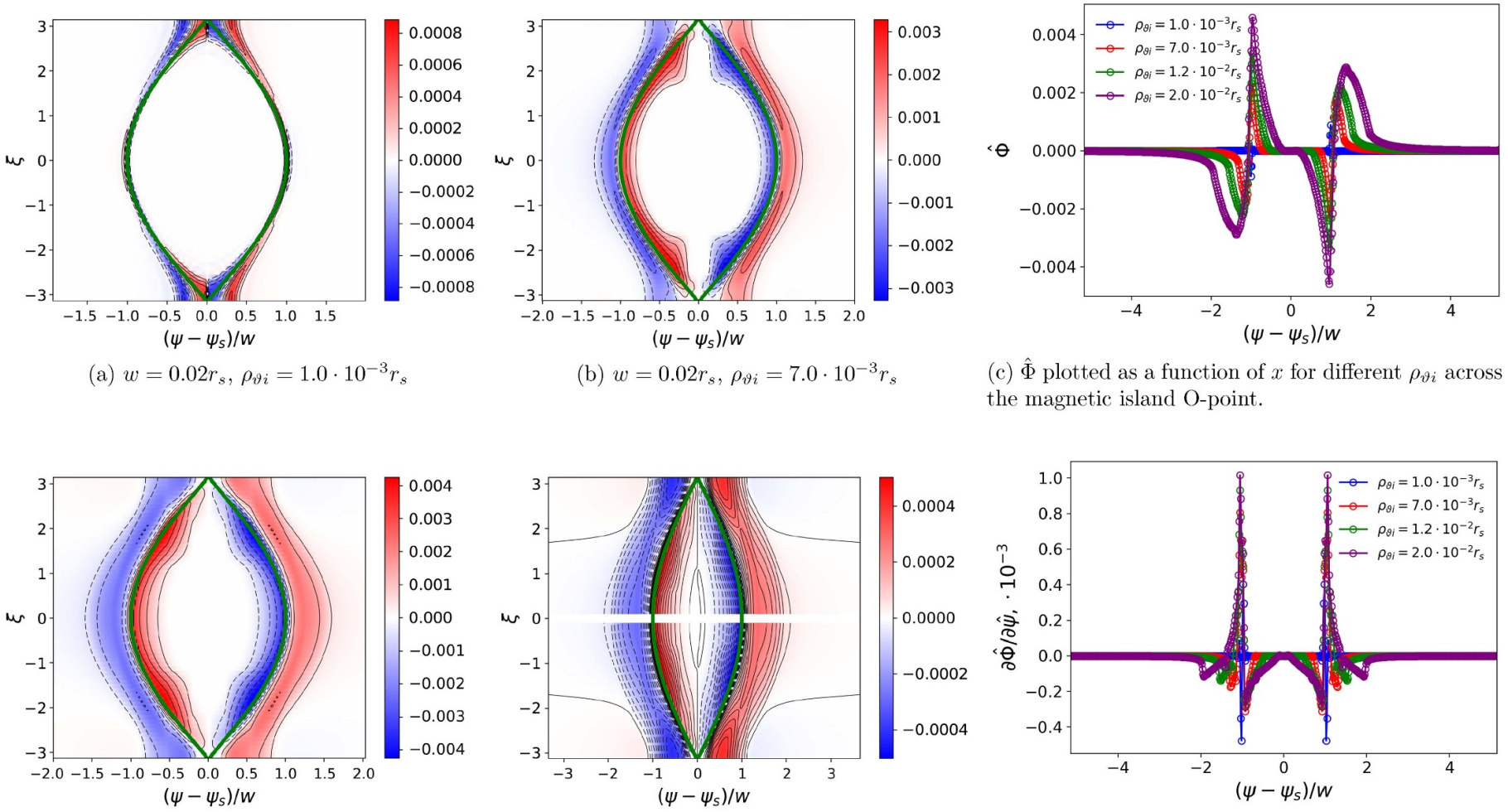

(a) $w = 0.02r_s$, $\rho_{\vartheta i} = 1.0 \cdot 10^{-3} r_s$

(b) $w = 0.02r_s$, $\rho_{\vartheta i} = 7.0 \cdot 10^{-3} r_s$

(c) $\hat{\Phi}$ plotted as a function of x for different $\rho_{\vartheta i}$ across the magnetic island O-point.

(d) $w = 0.02r_s$, $\rho_{\vartheta i} = 1.2 \cdot 10^{-2} r_s$

(e) $w = 0.02r_s$, $\rho_{\vartheta i} = 2.0 \cdot 10^{-2} r_s$

(f) $\partial\hat{\Phi}/\partial\psi$ plotted as a function of x for different $\rho_{\vartheta i}$ across the magnetic island O-point.

Figure 6. The electrostatic potential, $\hat{\Phi}$, as a function of x and ξ plotted at different $\rho_{\vartheta i}/w$. $w = 0.02r_s$, $\varepsilon = 0.1$, $\hat{L}_q = 1$, $L_B^{-1} = 0$, $L_n/L_{Ti} = 1$, $\nu_i^* = 10^{-3}$. The green line indicates the position of the magnetic island separatrix, $\Omega = 1$. (f) Radial electric field, $\partial\hat{\Phi}/\partial\hat{\psi}$, across the magnetic island O-point ($\xi = 0$) for different $\rho_{\vartheta i}$. The equilibrium density profile $\propto L_n^{-1}\hat{w}\hat{\psi}$, $\Phi'_{eqm} = 0$. $\partial_{\hat{\psi}}\hat{\Phi}_{\hat{\psi}\to\pm\infty} = 0$.

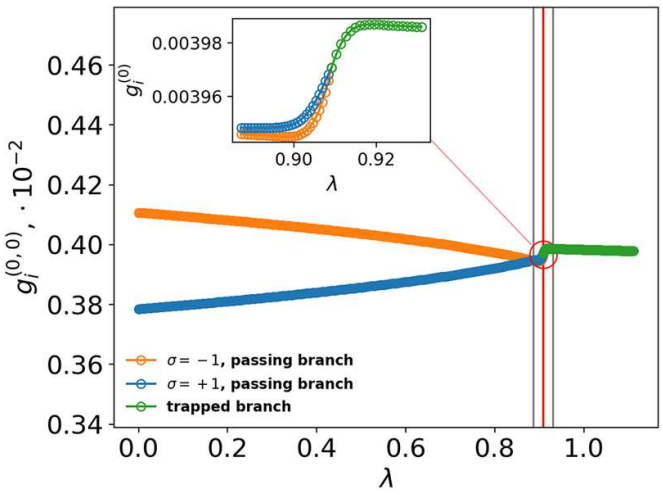

Figure 7. Leading order ion distribution function $g_i^{(0,0)}$ vs. pitch angle, λ, at $p_\varphi = 1.475w$, $\xi = 0$, $w = 0.02r_s$, $\rho_{\vartheta i} = 1.0 \times 10^{-3} r_s$, $\nu_i^* = 10^{-4}$, $\varepsilon = 0.1$, $\hat{L}_q = 1$. $g_i^{(0,0)}$ is normalised to $n_{eqm}/(\pi^{3/2} V_{Ti}^3)$. Inset: a full solution of equation (20) in a collisional layer around λ_c. The trapped branch solution is σ-independent at fixed $\hat{p}_\varphi$ due to the summation over σ in equation (16).

p_φ/ψ without introducing the layer explicitly. The introduction of this layer allows the particle distribution to vary on S contours and hence provides the freedom to impose the matching conditions, equations (106)–(108) of [18], at $\lambda = \lambda_c$.

Taking into account the narrowness of the dissipation layer, we fix all the coefficients in equation (14) at $\lambda_{p/t} \equiv \lambda_c \mp \epsilon$, where ε is the width of the layer. This is then equivalent to equation (20) with coefficients evaluated at $\lambda_{p/t}$ and S being replaced with $S = \hat{S} + \partial_\lambda S_{\lambda_{p/t}} (\lambda - \lambda_{p/t})$, where $\hat{S} = S(\lambda_{p/t})$. Exploiting the thinness of the layer again, we write:

$$\left.\frac{\partial}{\partial\lambda}\right|_\psi \simeq \left.\frac{\partial}{\partial\lambda}\right|_{p_\varphi} = \left.\frac{\partial}{\partial\lambda}\right|_{\hat{S}},$$

and thus within the layer our equation for $g_j^{(0)}$ becomes:

$$\mathcal{A}\left(\hat{S},\xi,\lambda_{p/t},V;\sigma\right)\left.\frac{\partial g_j^{(0)}}{\partial\xi}\right|_{\hat{S},\vartheta,\lambda,V} = \hat{\nu}_j \frac{2}{\hat{V}} a\left(\lambda_{p/t}\right)\left.\frac{\partial^2 g_j^{(0)}}{\partial\lambda^2}\right|_{\hat{S}}. \tag{26}$$

Here $\hat{\nu}_j$ is to be understood as ν_{ii}/V_{Ti} for ions and $(\nu_{ee}+\nu_{ei})/V_{Te}$ for electrons, and a is defined as $\left\langle \sigma\lambda(1-\lambda B)^{1/2} R/B_\varphi \right\rangle_\vartheta^{p_\varphi}$. Similar to [41], we replace ξ with an angle variable, $\gamma^{\pm/t}$, defined below, and hence equation (26) can be reduced to a simple diffusion equation:

$$\left.\frac{\partial g_j^{(0)}}{\partial\gamma^{\pm/t}}\right|_{\hat{S}} = D^{\pm/t}\left.\frac{\partial^2 g_j^{(0)}}{\partial\overline{\lambda}^2}\right|_{\hat{S}}, \tag{27}$$

where $D^{\pm/t} = (2\hat{\nu}_j/\hat{V}) a\left(\lambda_{p/t}\right)$ for passing, $\sigma = \pm 1$, and trapped branches. Here we have introduced:

$$\gamma^{out(\pm)/t} = \frac{\sigma_{p_\varphi}}{\int_{-\pi}^{\pi} \frac{d\xi}{2\pi|\mathcal{A}|}} \int_0^\xi \frac{d\xi'}{\mathcal{A}\left(\hat{S},\xi,V;\sigma\right)} \tag{28}$$

for passing particles outside the $\hat{S}$ island and for trapped particles. For passing particles inside the $\hat{S}$ island,

$$\gamma^{in(\pm)} = \frac{1}{\int_{-\xi_b}^{\xi_b} \frac{d\xi}{\pi|\mathcal{A}|}} \int_0^\xi \frac{d\xi'}{\mathcal{A}\left(\hat{S},\xi,V;\sigma\right)}, \qquad \sigma_{p_\varphi} > 0 \tag{29}$$

and

$$\gamma^{in(\pm)} = \pi - \frac{1}{\int_{-\xi_b}^{\xi_b} \frac{d\xi}{\pi|\mathcal{A}|}} \int_0^\xi \frac{d\xi'}{\mathcal{A}\left(\hat{S},\xi,V;\sigma\right)}, \qquad \sigma_{p_\varphi} < 0. \tag{30}$$

$\gamma^{\pm/t}$ has the same features as the angle variable introduced in [41]. $\overline{\lambda} = \left[\left\langle \mathcal{A}^{-1}\right\rangle_\xi^{\hat{S}}\right]^{-1/2}(\lambda - \lambda_c)$ is a new pitch angle variable. $\overline{\lambda} = 0$ defines the trapped-passing boundary; $\overline{\lambda} \lessgtr 0$ corresponds to the passing/trapped region, respectively. In contrast to [18], our layer solution includes both regions inside and outside the magnetic island. Equation (27) allows an analytic solution of the Fourier form: $g_j^{(0)} = \sum_{n\geq 0} C_n^{\pm/t} e^{\frac{i+1}{\sqrt{2}}\sqrt{\frac{n}{D^{\pm/t}}}\overline{\lambda}} e^{in\gamma^{\pm/t}}$ with $C_n^{\pm/t} = a_n^{\pm/t} + ib_n^{\pm/t}$. The Fourier coefficients, $a_n^{\pm/t}$, $b_n^{\pm/t}$ $(n \geq 0)$, are unknown and to be found from matching at $\overline{\lambda} = 0$:

$$\begin{aligned}
&H^+ + \sum_{n>0}\left\{a_n^+ \cos n\gamma^+ - b_n^+ \sin n\gamma^+\right\} = \\
&= H^- + \sum_{n>0}\left\{a_n^- \cos n\gamma^- - b_n^- \sin n\gamma^-\right\} = \\
&= H^t + \sum_{n>0}\left\{a_n^t \cos n\gamma^t - b_n^t \sin n\gamma^t\right\}, \\
&\sum_{n>0} \cos n\gamma^+ \sqrt{\frac{n}{2D^+}}\left[a_n^+ - b_n^+\right] - \sin n\gamma^+ \sqrt{\frac{n}{2D^+}}\left[a_n^+ + b_n^+\right] + \\
&+ \sum_{n>0} \cos n\gamma^- \sqrt{\frac{n}{2D^+}}\left[a_n^- + b_n^-\right] + \sin n\gamma^- \sqrt{\frac{n}{2D^+}}\left[a_n^- - b_n^-\right] = \\
&= 2\sum_{n>0} \cos n\gamma^t \sqrt{\frac{n}{2D^t}}\left[b_n^t - a_n^t\right] + \sin n\gamma^t \sqrt{\frac{n}{2D^t}}\left[a_n^t + b_n^t\right].
\end{aligned} \tag{31}$$

$H^{\pm/t}$ represents a sum of the drive term/contribution from outside the layer and the 0th harmonic, $a_0^{\pm/t}$ [39]. Equation (31) is a set of three equations for $6N+3$ unknowns, $n \in [0, N]$, where N represents the Fourier harmonics retained. Due to a difference in $\gamma^{\pm/t}$, matching at fixed ψ/p_φ cannot be provided in n space in the presence of Φ. However, $\gamma^{\pm/t}$ and n are conjugated variables, and $\gamma^{\pm/t}$ is connected with ξ via equations (28)–(30). Thus, taking a number of points in ξ space $N_\xi = 2\,\mathrm{N} + 1$ and treating $\gamma^{\pm/t} = \gamma^{\pm/t}\left(\hat{S},\xi,V\right) = \gamma^{\pm/t}\left[\hat{S}(\hat{p}_\varphi,\xi,V),\xi,V\right]$, we solve equation (31) numerically

for $a_n^{\pm/t}$, $b_n^{\pm/t}$, providing matching at fixed p_φ and ξ. Substituting the obtained Fourier coefficients into the above analytic solution in the layer provides matching across the trapped-passing boundary and is then to be used to provide the boundary condition required to solve for $g_j^{(0,0)}$ from equation (23).

In previous sections we have outlined the derivation of the orbit-averaged drift kinetic equation to leading order in Δ for ions and electrons that takes into account the electrostatic potential consistent with the plasma quasi-neutrality condition. Two numerical codes have been developed. One of them finds a solution of equation (14), which is a function of p_φ, ξ and λ and keeps collisions at leading order for a full range of λ variation. This is to be referred to as the DK-NTM solution and is explained in [36] and [42]. To introduce the drift islands explicitly for both electrons and ions and to efficiently resolve the collisional dissipation layer, the RDK-NTM solver has been developed to describe low collision frequency regimes [39]. It finds a solution of the reduced orbit-averaged drift kinetic equation to leading order in Δ, i.e. equation (14) in the dissipative layer and equation (23) outside the layer with the electrostatic potential consistent with plasma quasi-neutrality. The RDK-NTM numerical algorithm is described in [39]. The numerical results presented in this paper are provided by the RDK-NTM code. In appendix C we compare results from both models.

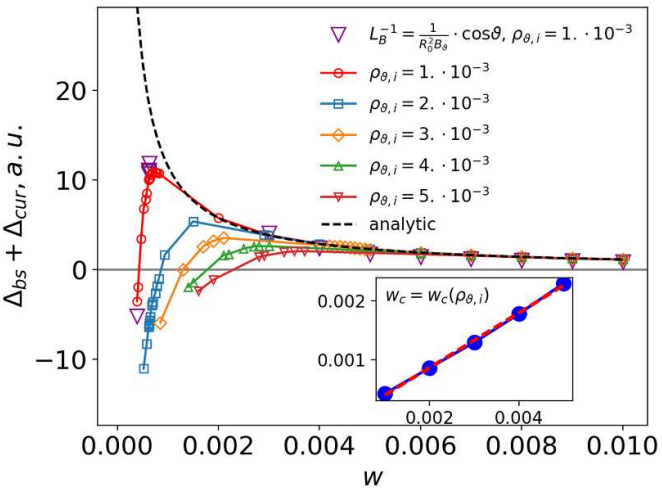

Figure 8. The sum of the bootstrap and curvature contributions to the MRE, $\Delta_{bs} + \Delta_{cur}$, vs. w for different values of the ion poloidal Larmor radius, $\rho_{\vartheta i}$, calculated with the RDK-NTM code. The dashed line is the analytic result for the bootstrap current contribution, valid in the limit of large magnetic island widths [18]. Here w_c, defined as a solution of $\Delta_{bs} + \Delta_{cur} = 0$, represents a magnetic island threshold, also called a critical magnetic island half-width. $\varepsilon = 0.1$, $\hat{L}_q = 1$, $L_B^{-1} = 0$, $\nu_i^* = 10^{-3}$. The equilibrium density and temperature gradients are $L_n/L_{Tj} = 1$, $\Phi'_{eqm} = 0$. Inset: w_c plotted against $\rho_{\vartheta i}$ (w, w_c and $\rho_{\vartheta i}$ here are in r_s units).

6. Neoclassical drive for NTMs

We can now return to equation (1) and consider how $J_\parallel$ contributes to the evolution of the magnetic island width. We note that equation (7) is equivalent to equation (1) provided a single isolated stationary NTM magnetic island is considered. Thus, for the stationary island, the classical tearing mode stability parameter, Δ', is balanced against the sum of all the neoclassical contributions, $\Delta' + \Delta_{neo} = 0$, where:

$$\Delta_{neo} = -\frac{\mu_0 R}{2\widetilde{\psi}} \int_{\mathbb{R}} d\psi \int_{-\pi}^{\pi} d\xi \bar{J}_\parallel \cos\xi. \tag{32}$$

Using the obtained ion/electron distribution function, we calculate $J_\parallel = \sum_j eZ_j u_{\parallel j}$. Defining the polarisation current density as the part of the parallel current density perturbation that flux surface averages to zero, we write:

$$\Delta_{bs} + \Delta_{cur} = -\frac{\mu_0 R}{2\widetilde{\psi}} \int_{\mathbb{R}} d\psi \int_{-\pi}^{\pi} d\xi \langle \bar{J}_\parallel \rangle_\xi^\Omega \cos\xi \tag{33}$$

for the sum of the bootstrap and curvature contributions and hence,

$$\Delta_{pol} = \Delta_{neo} - (\Delta_{bs} + \Delta_{cur}) \tag{34}$$

for the polarisation term. Here the ξ-averaging operator at fixed Ω is defined as:

$$\langle \ldots \rangle_\xi^\Omega = \frac{\oint \ldots (\Omega + \cos\xi)^{-1/2} d\xi}{\oint (\Omega + \cos\xi)^{-1/2} d\xi}, \tag{35}$$

similar to equation (24). As we mentioned earlier, we focus on a large aspect ratio, circular cross section tokamak approximation here, and employ our 3D RDK-NTM code to analyse the threshold physics. Since $\Delta_{cur} = \mathcal{O}(\varepsilon^2)$, it does not provide a significant contribution to the threshold obtained in this work. In particular, $\Delta_{bs} + \Delta_{cur}$ reduces to the bootstrap current contribution for magnetic islands in the limit of large widths, $w \gg \rho_{\vartheta i}$.

In figure 8 we plot $\Delta_{bs} + \Delta_{cur}$ against w. In the limit of $w \gg \rho_{\vartheta i}$, $\Delta_{bs} + \Delta_{cur}$ is inversely proportional to w, which is expected from the existing analytic theory, e.g. equation (85) of [18]. When w tends to zero, $\Delta_{bs} + \Delta_{cur}$ becomes negative, providing a threshold for NTMs, i.e. a value of w below which the mode is stable, $\Delta_{bs} + \Delta_{cur} < 0$. This value is denoted by w_c and is to be referred to as the critical magnetic island half-width. w_c is different for each ion poloidal Larmor radius and hence can be defined as a function of $\rho_{\vartheta i}$. This kind of behaviour at $w \sim \rho_{\vartheta i}$ is the direct result of the inclusion of the drift islands in our model and is in agreement (qualitative and quantitative) with experimentally observed self-healing of small magnetic islands below the threshold (e.g. [33]). A straight line fit shown in the inset of figure 8. provides $w_c = 0.46\rho_{\vartheta i}$ and in terms of the ion banana width $w_c = 1.47\rho_{bi}$ at $\varepsilon = 0.1$ (here w_c, $\rho_{\vartheta i}$ and ρ_{bi} are normalised to r_s). $w_c/\rho_{\vartheta i}$ as a function of ε is shown in figure 9, which indicates that the banana width is the appropriate measure. Recall that experimentally it was found that the full critical magnetic island width is between $(2,3)\rho_{bi}$, so this result is in the right vicinity. In previous work [36] we found a much larger threshold

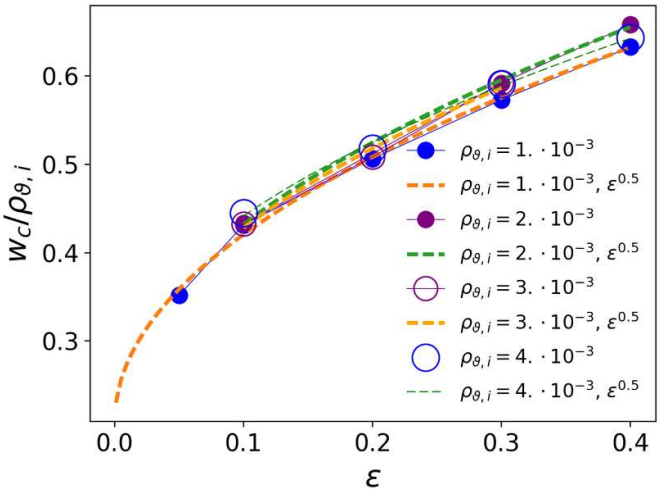

Figure 9. $w_c/\rho_{\vartheta i}$ as a function of ε. The parameters are chosen as in figure 8. w_c here is based on the bootstrap contribution only. The $\varepsilon^{1/2}$ behavior provides the best fit.

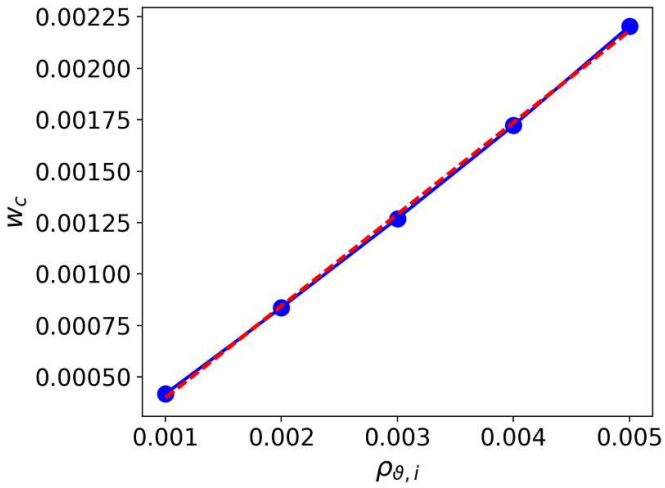

Figure 10. The full critical magnetic island width, w_c, as a function of the ion poloidal Larmor radius, $\rho_{\vartheta i}$. The red dashed line is the best fit line that provides the approximation. w_c and $\rho_{\vartheta i}$ are normalised to the radius of the rational surface, r_s. The parameters are chosen as in figure 8.

$w_c \simeq 9\rho_{bi}$, but there we had a larger magnetic drift frequency—the value chosen here, with $L_B^{-1} = 0$, is closer to the experimental case[10]. This highlights an additional sensitivity of w_c to L_B.

When the island propagation frequency is close to zero, the polarisation current contribution is expected to be small. Indeed, we find that inclusion of Δ_{pol} at $\omega = 0$ does not shift the threshold significantly falling slightly to $w_c = 1.41\rho_{bi}$. The latter is obtained in the conventional tokamak geometry with $\varepsilon = 0.1$ in the absence of the Shafranov shift, plasma elongation and triangularity (equilibrium density and temperature gradients are $L_n/L_{Tj} = 1$ with $\Phi'_{eqm} = 0$). The threshold we derive is the result of the radial shift of drift islands described by the S function, equation (21), and, in particular, the pressure gradient restoration across the magnetic island O-point at $w \sim \rho_{\vartheta i}$. As discussed in section 5, the latter mainly arises from the behaviour of the σ-dependent part of the ion distribution function, $\sum_\sigma g_i^{(0,0),\sigma}$, at small w. Therefore, we emphasise that this threshold physics is related to passing particle dynamics, and not the finite banana width effects of the trapped particles.

7. Summary and conclusions

To summarise, a new drift kinetic theory of magnetic islands, valid for $w \sim \rho_{\vartheta i}$, has been developed in a low collisionality plasma. The electron/ion distribution function is found to be flattened across the so called drift islands, which are radially shifted by a value, proportional to $\rho_{\vartheta e/i}/w$, compared to the magnetic island. This, in turn, results in a density gradient being sustained across a magnetic island of width comparable to the ion poloidal Larmor radius, $w \lesssim \rho_{\vartheta i}$. For ions, their finite density gradient at the centre of the magnetic island is the consequence of the effect of the drift islands, i.e. the relatively large radial shift in equation (21). While the electron radial shift is small since $\rho_{\vartheta e} \ll \rho_{\vartheta i}$, their density gradient is still present across the magnetic island O-point due to the effect of the electrostatic potential that is generated to ensure plasma quasi-neutrality.

This gradient is found to suppress the drive for NTMs when w is small, providing the critical magnetic island width, below which NTMs decay. We note that this physics is associated with the passing particle dynamics and not the effects of the finite banana orbit width. In this sense, the relevant parameter for the NTM threshold would be the ion poloidal Larmor radius. However, we find that in addition to the linear dependence of w_c on $\rho_{\vartheta i}$, w_c also scales with the inverse aspect ratio as $\varepsilon^{1/2}$. This indicates that the threshold is also influenced by the trapped particles—this is physics that we do not yet fully understand. For the small inverse aspect ratio circular poloidal cross section tokamak, it scales as $w_c = 0.45\rho_{\vartheta i}$ at $\varepsilon = 0.1$ in the island rest frame. This provides $w_c = 1.41\rho_{bi}$, if written in terms of the ion banana orbit width. This result is in quantitative agreement with the previous experimental observations, e.g. [33].

If we consider contours of the total density, obtained with the self-consistent electrostatic potential and differentiated with respect to ψ, we notice that these contours in the (ψ, ξ) plane would reproduce the contours of the flow parallel to the field lines. This changes abruptly with $\rho_{\vartheta i}/w$, as can be seen from figures 4(a)–(d). Therefore, comparing the total density profiles that contain the magnetic island perturbation against the experimental density profiles for a large magnetic island and for a small island near the marginal stability might be one of the steps to check the validity of the drift island concept as an explanation of the threshold, w_c.

[10] As shown in appendix A, the $(1/B)\partial B/\partial\psi$ term is ε times smaller than the rest of the terms kept in equations (14) and (15). Therefore, $L_B^{-1} = 0$ provides results, close to the case when the actual ϑ dependence is maintained in L_B, which we can see from figure 8.

The theory presented here provides a prediction for the magnetic island threshold obtained in the conventional tokamak limit in the island rest frame. However, as mentioned above, the theory presented in this paper is subject to certain limitations. One of them is the boundary layer around the drift island separatrix. In this layer, the transport terms will become comparable to the parallel streaming, i.e. the left hand side of equation (20), $\nu_{ii/e}\partial^2/\partial S^2 \sim \mathcal{A}\partial/\partial\xi|_S$. This layer can be treated in a similar way to the collisional dissipative layer at the trapped-passing boundary, which we considered in section 5 by exploiting its thinness. However, as the drift islands are shifted radially relative to the magnetic island by an amount that varies with $V_\parallel$ and is proportional to $\rho_{\vartheta j}$, this might result in a broader layer around the magnetic island for the electrostatic potential, being spread over a width comparable to $\rho_{\vartheta j}$. It is this layer in the potential that influences the polarisation current when ω is not equal to zero. We will present this in future publications, extending existing theories of the separatrix layer [21, 22, 29, 30]. A special challenge is where both boundary layers overlap, $\mathcal{A}\partial/\partial\xi|_S \sim \nu_{ii/e}\partial^2/\partial\lambda^2 \sim \nu_{ii/e}\partial^2/\partial S^2$. However, since this area is very narrow in the low collisionality plasma, we can fix all the coefficients in the full equation, equation (14), and thus find the solution even in the presence of the electrostatic potential in a way similar to section 5. The obvious advantage of this method, employed in RDK-NTM, is that it allows us to obtain the solution with sufficient resolution in these narrow boundary regions. Another option to deal with the separatrix layer in S space is to solve equation (14) for the full 4D distribution function as a function of p_φ, ξ and λ at each V. This is the DK-NTM approach, presented in appendix C. However, as mentioned above, it is then difficult to efficiently resolve both layers simultaneously and there are numerical limits to how small we can take ν_j or $\rho_{\vartheta i}/w$. For the collision operator employed in this paper, which captures aspects of neoclassical transport, the thinness of the boundary layer that surrounds the drift island is provided by low $\nu_{ii/e}$. More generally, the cross-field transport will be driven by turbulence, and then the layer physics will be much more complicated to capture, especially as the island and the layer length scales become comparable to turbulent eddy size—this will become a challenging multiscale numerical problem. Both the 3D and 4D approaches have their benefits and drawbacks, and both require extra development to refine the treatment of the separatrix layers. We highlight that while the proper treatment of the separatrix boundary layer is necessary for calculating accurately the layer contribution to the polarisation current, this does not influence the bootstrap current. Thus, the result presented here for the NTM threshold when the island is at rest in the plasma $\boldsymbol{E}\times\boldsymbol{B}$ reference frame is expected to be robust.

The second problem that is beyond the scope of this paper is the calculation of the island rotation frequency [39]. This is associated with the dissipation processes in the plasma. In [39] it is found from the solution in the dissipation layer around the trapped-passing boundary, provided it is the main source of dissipation. Potentially, there might be an extra contribution from the separatrix layer and thus is to be further investigated. While the bootstrap current perturbation described here is not expected to depend on the island propagation frequency, the polarisation current will, and this could influence the threshold.

Another problem to be addressed in the future is the curvature contribution to the island evolution. The drift kinetic equation presented in this paper is correct to $\mathcal{O}(\varepsilon^2\Delta g_j)$, which is already sufficient to find Δ_{cur}. The more accurate calculation, though, would also require the $\mathcal{O}(\varepsilon^2\Delta^2 g_j)$ terms. We highlight that while the effects of the plasma shaping are weak in conventional devices, they would be more important for spherical tokamaks and potentially further enhance the stabilising mechanisms that provide a threshold.

Data accessibility statement

The DK- and RDK-NTM numerical data used for benchmarking is available at https://doi.org/10.5281/zenodo.4294044.

Acknowledgments

This work was supported by the UK Engineering and Physical Sciences Research Council, Grant No. EP/N009363/1. Numerical calculations were performed using the ARCHER computing service through the Plasma HEC Consortium EPSRC Grant No. EP/R029148/1. This work has been carried out within the framework of the EUROfusion Consortium and has received funding from the Euratom research and training programme 2014–2018 and 2019–2020 under Grant Agreement No. 633053. The views and opinions expressed herein do not necessarily reflect those of the European Commission.

Appendix A. The $\mathcal{O}(\varepsilon^{2(5/2)}\Delta g_j)$ form of equation (14). Expression for $\partial B/\partial\psi$

The general form of equation (14) is:

$$\left[\underbrace{\frac{q_s'}{q_s}p_\varphi\Theta(\lambda_c-\lambda)}_{①}+\underbrace{\frac{q_s'}{q_s}\left\langle\frac{IV_\parallel}{\omega_{cj}}\right\rangle^{p_\varphi}_{\vartheta}}_{②}+\left\langle\frac{B^2}{B_\varphi^2}\frac{I}{\omega_{cj}}\frac{\partial B}{B\partial\psi}\left(\underbrace{V_\parallel}_{③}+\underbrace{\frac{\lambda BV^2}{2V_\parallel}}_{④}\right)\right\rangle^{p_\varphi}_{\vartheta}+\left\langle\frac{R^2B_\vartheta^2}{I}\vartheta'\underbrace{\frac{\partial}{\partial\vartheta}\bigg|_{\psi,\xi}}_{⑤}\left(\frac{V_\parallel}{\omega_{cj}}\right)\right\rangle^{p_\varphi}_{\vartheta}-\left\langle\frac{R^2B}{IV_\parallel}\underbrace{\frac{\partial\Phi}{\partial\psi}\bigg|_{\vartheta,\xi}}_{⑥}\right\rangle^{p_\varphi}_{\vartheta}\right]\times$$

$$\times \left.\frac{\partial g_j^{(0)}}{\partial \xi}\right|_{p_\varphi,\vartheta} + \left[\underbrace{\left\langle \frac{R^2}{I}\left(\boldsymbol{B}_1\cdot\boldsymbol{\nabla} p_\varphi\right)\right\rangle_\vartheta^{p_\varphi}}_{⑦} + \right.$$

$$\left. + \underbrace{\left\langle \frac{R^2 B}{I V_\parallel}\left.\frac{\partial \Phi}{\partial \xi}\right|_{\psi,\vartheta}\right\rangle_\vartheta^{p_\varphi}}_{⑧}\right] \left.\frac{\partial g_j^{(0)}}{\partial p_\varphi}\right|_{\vartheta,\xi} = \left\langle \frac{R^2 B}{I V_\parallel} C_j\right\rangle_\vartheta^{p_\varphi} g_j^{(0)} \tag{A1}$$

to $\mathcal{O}(\varepsilon^{2(5/2)}\Delta g_j)$, which can be obtained directly from equation (11)[11]. The rest will provide the $\mathcal{O}(\Delta^2 g_j)$ or smaller corrections. Here the second term in equation (15) has been rearranged using:

$$\left.\frac{\partial}{\partial \psi}\right|_{\vartheta,\xi}\left(\frac{V_\parallel}{B}\right) = -\frac{1}{B}\frac{\partial B}{\partial \psi}\left(\frac{\lambda V^2}{2V_\parallel} + \frac{V_\parallel}{B}\right).$$

For $\partial B/\partial\psi$ we have,

$$\frac{\partial B}{\partial \psi} = \frac{I'}{R} - \frac{I}{R^2}\frac{\partial R}{\partial \psi}$$

with $I' \sim R^2 p'/I$ and hence $I'/R \sim \beta/r^2$. Thus, in a low beta limit, we find,

$$\frac{\partial B}{\partial \psi} = -\frac{B_\varphi}{R_0^2 B_\vartheta}\cos\vartheta + \mathcal{O}(\varepsilon^2/r^2) \tag{A2}$$

with $R = R_0(1+\varepsilon\cos\vartheta)$ taken for the model major radius. Estimating each of the terms in equation (A1), we find,

$$① + ② \sim \frac{q_s'}{q_s}\left\langle p_\varphi + \frac{I V_\parallel}{\omega_{cj}}\right\rangle_\vartheta^{p_\varphi}\frac{\partial g_j}{\partial \xi} \sim \frac{q_s'}{q_s}\frac{m-nq}{-nq_s'} g_j$$
$$\sim \left(1 - \frac{q}{q_s}\right) g_j \sim \Delta g_j,$$

$$③ \sim ④ \sim \varepsilon \Delta g_j,$$
$$② \sim \varepsilon^2 \Delta g_j,$$
$$⑥ \sim ⑦ \sim ⑧ \sim \Delta g_j.$$

Here $\partial_\vartheta(V_\parallel/\omega_{cj}) \sim \partial\rho_{\vartheta j}/\partial\vartheta \sim \varepsilon\rho_{\vartheta j}$ for passing and $\sim \varepsilon^{3/2}\rho_{\vartheta j}$ for trapped particles. Omitting the $\mathcal{O}(\varepsilon^2\Delta g_j)$ corrections in $\partial B/\partial\psi$ and in equation (A1), we find equation (14).

Appendix B. Collision operator averaging

Rewriting equation (14) in terms of the normalised quantities given by equation (19), we obtain equations (20) and (21), where the dimensionless magnetic drift frequency is:

$$\hat{\omega}_D = -\frac{\hat{w}}{\hat{L}_q}\left\langle \hat{V}_\parallel\right\rangle_\vartheta^{p_\varphi} + \left\langle \frac{B^2}{B_\varphi^2}\frac{\hat{w}}{\hat{L}_B}\left[\hat{V}_\parallel + \frac{\lambda \hat{V}^2}{2\hat{V}_\parallel}B\right]\right\rangle_\vartheta^{p_\varphi}. \tag{B1}$$

We employ the same collision operator, C_j, as described in equations(62) of [18], i.e.

$$C_j g_i = \nu_j(V)\left[2\frac{(1-\lambda B)^{1/2}}{B}\left.\frac{\partial}{\partial\lambda}\right|_\psi\left(\lambda(1-\lambda B)^{1/2}\left.\frac{\partial g_j}{\partial\lambda}\right|_\psi\right) + \right.$$
$$\left. + \frac{V_\parallel \hat{u}_{\parallel j}(g_j)}{V_{Tj}^2} f_j^M\right]. \tag{B2}$$

For ions, $\nu_i = \nu_{ii}(V) = \nu_{ii}(V_{Ti})(V_{Ti}/V)^3$ and the momentum-conserving *flow* term is $\hat{u}_{\parallel i} = \bar{u}_{\parallel i}(g_i)$. Ion-electron collisions are small and hence neglected. For electrons, $\nu_e = \nu_{ee}(V) + \nu_{ei}(V)$ with $\nu_{ej}(V) = \nu_{ej}(V_{Te})(V_{Te}/V)^3$, $j = e, i$, and the flow term is $\hat{u}_{\parallel e} = (\nu_{ee}/\nu_e)\bar{u}_{\parallel e}(g_e) + 2(\nu_{ei}/\nu_e)u_{\parallel i}(g_i)$. Here we have introduced $\bar{u}_{\parallel j} = (3\pi^{1/2})/(2n_{eqm})V_{Tj}^3\int d\boldsymbol{V} g_j V_\parallel/V^3$, $j = e, i$, and $u_{\parallel i}$ was defined in section 5.

Since $\partial/\partial\lambda|_\psi$ and $\langle\ldots\rangle_\vartheta^{p_\varphi}$ are not commutative, we transform the pitch angle derivatives, using

$$\left.\frac{\partial}{\partial\lambda}\right|_\psi = \left.\frac{\partial}{\partial\lambda}\right|_{\hat{p}_\varphi} + \left.\frac{\partial \hat{p}_\varphi}{\partial\lambda}\right|_\psi \left.\frac{\partial}{\partial \hat{p}_\varphi}\right|_\lambda \tag{B3}$$

and

$$\left.\frac{\partial}{\partial\lambda}\right|_{\hat{p}_\varphi} = \left.\frac{\partial}{\partial\lambda}\right|_S + \left.\frac{\partial S}{\partial\lambda}\right|_{\hat{p}_\varphi}\left.\frac{\partial}{\partial S}\right|_\lambda \tag{B4}$$

with $\partial\hat{p}_\varphi/\partial\lambda|_\psi \equiv p_\lambda(\vartheta,\lambda,V;\sigma)$. Equation (B3) allows us to write:

$$\left\langle \left.\frac{\partial}{\partial\lambda}\right|_\psi\left(\sigma\lambda(1-\lambda B)^{1/2}\frac{R}{B_\varphi}\left.\frac{\partial g_j^{(0)}}{\partial\lambda}\right|_\psi\right)\right\rangle_\vartheta^{p_\varphi} =$$
$$= \left\langle \sigma\lambda\sqrt{1-\lambda B}\frac{R}{B_\varphi}\right\rangle_\vartheta^{p_\varphi}\left.\frac{\partial^2 g_j^{(0)}}{\partial\lambda^2}\right|_{\hat{p}_\varphi} +$$
$$+ \left\langle \sigma\frac{2-3\lambda B}{2\sqrt{1-\lambda B}}\frac{R}{B_\varphi}\right\rangle_\vartheta^{p_\varphi}\left.\frac{\partial g_j^{(0)}}{\partial\lambda}\right|_{\hat{p}_\varphi} +$$
$$+ \left\langle \sigma\frac{\hat{\rho}_{\vartheta j}^2}{4}\frac{\hat{V}^2 B^2\lambda}{\sqrt{1-\lambda B}}\frac{R}{B_\varphi}\right\rangle_\vartheta^{p_\varphi}\left.\frac{\partial^2 g_j^{(0)}}{\partial\hat{p}_\varphi^2}\right|_\lambda +$$
$$+ \left\langle \frac{\hat{\rho}_{\vartheta j}}{2}\hat{V}R\right\rangle_\vartheta^{p_\varphi}\left.\frac{\partial g_j^{(0)}}{\partial\hat{p}_\varphi}\right|_\lambda +$$
$$+ \left\langle \hat{\rho}_{\vartheta j}\hat{V}R\lambda\right\rangle_\vartheta^{p_\varphi}\left.\frac{\partial}{\partial\lambda}\right|_{\hat{p}_\varphi}\left(\left.\frac{\partial g_j^{(0)}}{\partial\hat{p}_\varphi}\right|_\lambda\right). \tag{B5}$$

Then applying equation (B4) to switch from $\hat{p}_\varphi$ to S, we obtain:

$$\left\langle \left.\frac{\partial}{\partial\lambda}\right|_\psi\left(\sigma\lambda(1-\lambda B)^{1/2}\frac{R}{B_\varphi}\left.\frac{\partial g_j^{(0)}}{\partial\lambda}\right|_\psi\right)\right\rangle_\vartheta^{p_\varphi} =$$
$$= \left\langle \sigma\lambda\sqrt{1-\lambda B}\frac{R}{B_\varphi}\right\rangle_\vartheta^{p_\varphi}\left.\frac{\partial^2 g_j^{(0)}}{\partial\lambda^2}\right|_{S,\xi} +$$
$$+ \left\langle \sigma\frac{2-3\lambda B}{2\sqrt{1-\lambda B}}\frac{R}{B_\varphi}\right\rangle_\vartheta^{p_\varphi}\left.\frac{\partial g_j^{(0)}}{\partial\lambda}\right|_{S,\xi} + C_{SS}\left.\frac{\partial^2 g_j^{(0)}}{\partial S^2}\right|_{\lambda,\xi} +$$
$$+ C_S\left.\frac{\partial g_j^{(0)}}{\partial S}\right|_{\lambda,\xi} + C_{\lambda S}\left.\frac{\partial^2 g_j^{(0)}}{\partial\lambda\partial S}\right|_\xi. \tag{B6}$$

[11] $\varepsilon^{5/2}$ corresponds to trapped particles.

Here

$$C_{SS}=\left\langle \sigma\lambda\sqrt{1-\lambda B}\frac{R}{B_\varphi}\right\rangle_\vartheta^{p_\varphi}\left(\left.\frac{\partial S}{\partial\lambda}\right|_{\hat p_\varphi,\xi}\right)^2+\left\langle\hat\rho_{\vartheta j}\hat V R\lambda\right\rangle_\vartheta^{p_\varphi}\left.\frac{\partial S}{\partial\lambda}\right|_{\hat p_\varphi,\xi}\left.\frac{\partial S}{\partial\hat p_\varphi}\right|_{\xi,\lambda}+$$
$$+\left\langle\sigma\frac{\hat\rho_{\vartheta j}^2}{4}\frac{\hat V^2B^2\lambda}{\sqrt{1-\lambda B}}\frac{R}{B_\varphi}\right\rangle_\vartheta^{p_\varphi}\left(\left.\frac{\partial S}{\partial\hat p_\varphi}\right|_{\xi,\lambda}\right)^2,$$
$$C_S=\left\langle \sigma\lambda\sqrt{1-\lambda B}\frac{R}{B_\varphi}\right\rangle_\vartheta^{p_\varphi}\left(\left.\frac{\partial}{\partial\lambda}\right|_{S,\xi}\left(\left.\frac{\partial S}{\partial\lambda}\right|_{\hat p_\varphi,\xi}\right)+\left.\frac{\partial S}{\partial\lambda}\right|_{\hat p_\varphi,\xi}\left.\frac{\partial}{\partial S}\right|_{\lambda,\xi}\left(\left.\frac{\partial S}{\partial\lambda}\right|_{\hat p_\varphi,\xi}\right)\right)+$$
$$+\left\langle\sigma\frac{2-3\lambda B}{2\sqrt{1-\lambda B}}\frac{R}{B_\varphi}\right\rangle_\vartheta^{p_\varphi}\left.\frac{\partial S}{\partial\lambda}\right|_{\hat p_\varphi,\xi}+\left\langle\sigma\frac{\hat\rho_{\vartheta j}^2}{4}\frac{\hat V^2B^2\lambda}{\sqrt{1-\lambda B}}\frac{R}{B_\varphi}\right\rangle_\vartheta^{p_\varphi}\left.\frac{\partial S}{\partial\hat p_\varphi}\right|_{\xi,\lambda}\left.\frac{\partial}{\partial S}\right|_{\lambda,\xi}\left(\left.\frac{\partial S}{\partial\hat p_\varphi}\right|_{\xi,\lambda}\right)+$$
$$+\frac12\left\langle\hat\rho_{\vartheta j}\hat V R\lambda\right\rangle_\vartheta^{p_\varphi}\left.\frac{\partial}{\partial\lambda}\right|_{S,\xi}\left(\left.\frac{\partial S}{\partial\hat p_\varphi}\right|_{\xi,\lambda}\right)+\frac12\left\langle\hat\rho_{\vartheta j}\hat V R\lambda\right\rangle_\vartheta^{p_\varphi}\left.\frac{\partial S}{\partial\lambda}\right|_{\hat p_\varphi}\left.\frac{\partial}{\partial S}\right|_{\lambda,\xi}\left(\left.\frac{\partial S}{\partial\hat p_\varphi}\right|_{\xi,\lambda}\right)+$$
$$+\frac12\left\langle\hat\rho_{\vartheta j}\hat V R\lambda\right\rangle_\vartheta^{p_\varphi}\left.\frac{\partial S}{\partial\hat p_\varphi}\right|_{\xi,\lambda}\left.\frac{\partial}{\partial S}\right|_{\lambda,\xi}\left(\left.\frac{\partial S}{\partial\lambda}\right|_{\hat p_\varphi}\right)+\left\langle\frac{\hat\rho_{\vartheta j}}{2}\hat V R\right\rangle_\vartheta^{p_\varphi}\left.\frac{\partial S}{\partial\hat p_\varphi}\right|_{\xi,\lambda},$$
$$C_{\lambda S}=2\left\langle\sigma\lambda\sqrt{1-\lambda B}\frac{R}{B_\varphi}\right\rangle_\vartheta^{p_\varphi}\left.\frac{\partial S}{\partial\lambda}\right|_{\hat p_\varphi,\xi}+\left\langle\hat\rho_{\vartheta j}\hat V R\lambda\right\rangle_\vartheta^{p_\varphi}\left.\frac{\partial S}{\partial\hat p_\varphi}\right|_{\xi,\lambda}.$$

The first two terms in equation (B6) will provide the pitch angle scattering in S space, while the other three terms are responsible for transport across surfaces of fixed S. Substituting equation (B6) into the above collision operator provides $\hat C_j$ and hence the collisional constraint in S space, equation (23). After multiplying both sides of equation (23) by $\hat V/2\hat\nu_{ii}$, the momentum conservation terms in equation (23) become $\frac{\hat V_i}{2}\left\langle\frac{1}{\mathcal A}\bar U_{\|i}(g_i^{(0,0)})\right\rangle_\xi^S$ for ions and $\frac{\hat V_e}{2}\left\langle\frac{1}{\mathcal A}\bar U_{\|e}(g_e^{(0,0)})\right\rangle_\xi^S+\frac{\hat V_e}{2}\left\langle\frac{1}{\mathcal A}U_{\|ei}(g_i^{(0,0)})\right\rangle_\xi^S$ for electrons, $\hat V_j=V/V_{Tj}$. Here

$$\bar U_{\|i}(g_i^{(0,0)})=\frac32e^{-\hat V_i^2}\left\langle RB_0\sum_\sigma\sigma\int_{\mathbb{R}+}d\hat V_i\int_0^{B^{-1}}g_i^{(0,0)}d\lambda\right\rangle_\vartheta^{p_\varphi},$$
$$\bar U_{\|e}(g_e^{(0,0)})=\frac32e^{-\hat V_e^2}\frac{\hat\nu_{ee}}{\hat\nu_{ee}+\hat\nu_{ei}}\left\langle B_0^2\frac{R}{B_\varphi}\sum_\sigma\sigma\int_{\mathbb{R}+}d\hat V_e\int_0^{B^{-1}}g_e^{(0,0)}d\lambda\right\rangle_\vartheta^{p_\varphi}$$

and

$$U_{\|ei}(g_i^{(0,0)})=\frac{2}{\pi^{1/2}}e^{-\hat V_e^2}\left(\frac{m_e}{m_i}\right)^2\frac{\hat\nu_{ei}}{\hat\nu_{ee}+\hat\nu_{ei}}\left\langle\frac{R}{B_\varphi}B_0^2\sum_\sigma\sigma\int_{\mathbb{R}+}d\hat V_i\hat V_i^3\int_0^{B^{-1}}g_i^{(0,0)}d\lambda\right\rangle_\vartheta^{p_\varphi}.$$

Appendix C. Benchmarking of the (4D) DK-and (3D) RDK-NTM models for the plasma response to a magnetic island

In this appendix we compare the 4D DK-NTM model with our new 3D RDK-NTM model in the relevant limit of low collision frequency. Note that the current DK-NTM version does not contain iterations on the electrostatic potential. The fully consistent DK-NTM approach is currently under development and shall be presented in the future.

In figures C1(a) and (b) we compare the (R)DK-NTM solutions plotted against y, where $y=\sqrt{S-S_{\min}}$ with $S_{\min}$ being a minimum value of S as a function of $\hat p_\varphi$, ξ, λ, $\hat V$ for each σ. $S=S_{\min}$ therefore corresponds to the O-point of the drift island. We see that the models are in agreement, even approaching $\lambda=\lambda_c$ ($\lambda_c=0.91$ for $\varepsilon=0.1$). In figures C1(c)–(h) we plot the DK-NTM solution outside and inside the collisional dissipative layer around the trapped-passing boundary. As we can see from figures C1(c)–(e), the ξ dependence of $g_j^{(0)}$ in y/S space is indeed weak at the deeply passing end and becomes significant only when λ enters the collisional dissipation layer (figures C1(f)–(h)), consistent with the S formalism developed in section 5 for the RDK-NTM model. In figures C2–C3 we plot the DK- and RDK-NTM density moments, $(1/2)\sum_\sigma g_i^{(0),\sigma}$, against p_φ across the O-point and X-point in ξ space. In λ space two points are chosen: well in the passing region and in the vicinity of the trapped-passing boundary, where the collisional layer influences the solution. Note the oscillations in the vicinity of the X-point produced

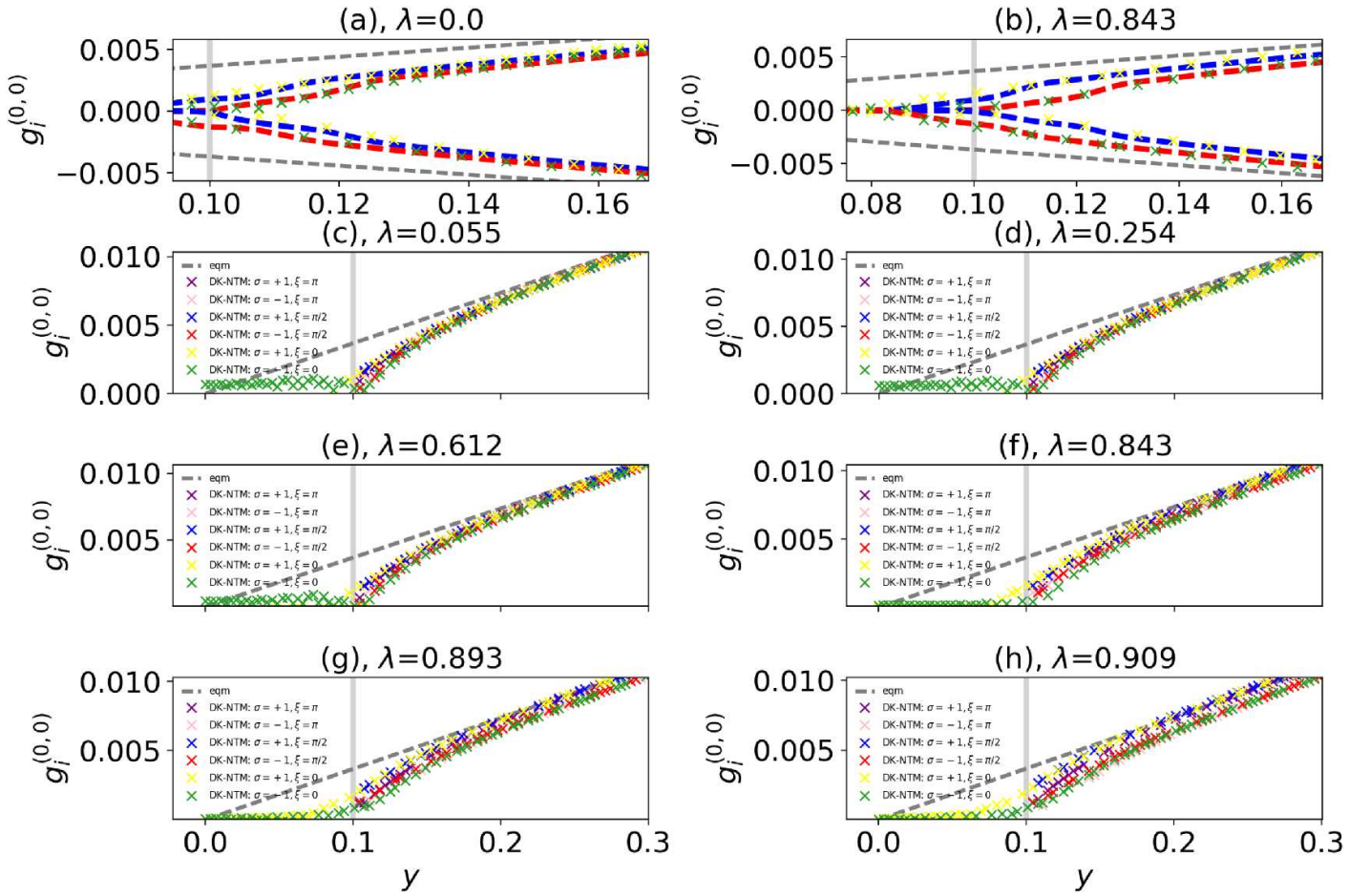

Figure C1. The leading order ion distribution function, $g_i^{(0)}$, plotted against y at different λ in the absence of Φ. (a),(b): zoom in the vicinity of the S island separatrix, $y = 0.1$, denoted by the grey vertical line. The green ($\sigma = -1$) and yellow ($\sigma = +1$) markers denote the DK-NTM solution. The red ($\sigma = -1$) and blue ($\sigma = +1$) dashed curves correspond to the RDK-NTM solution, $g_i^{(0,0)}$. The grey dashed line is the equilibrium in the absence of the island. (c)–(e) and (f)–(h) show solutions outside and inside the dissipative layer, respectively, for the DK-NTM model. $\sigma_{p_\varphi} > / < 0$ in the right/left of the drift island. $g_i^{(0,0)}$ is normalised to $n_{eqm}/(\pi^{3/2}V_{Ti}^3)$. $w = 0.02r_s$, $\rho_{\vartheta i} = 1.0 \cdot 10^{-3} r_s$, $\nu_i^* = 10^{-2}$, $\varepsilon = 0.1$, $\lambda_c = 0.91$, $\hat{L}_q = 1$, $L_n = 1$, $\Phi'_{eqm} = 0$.

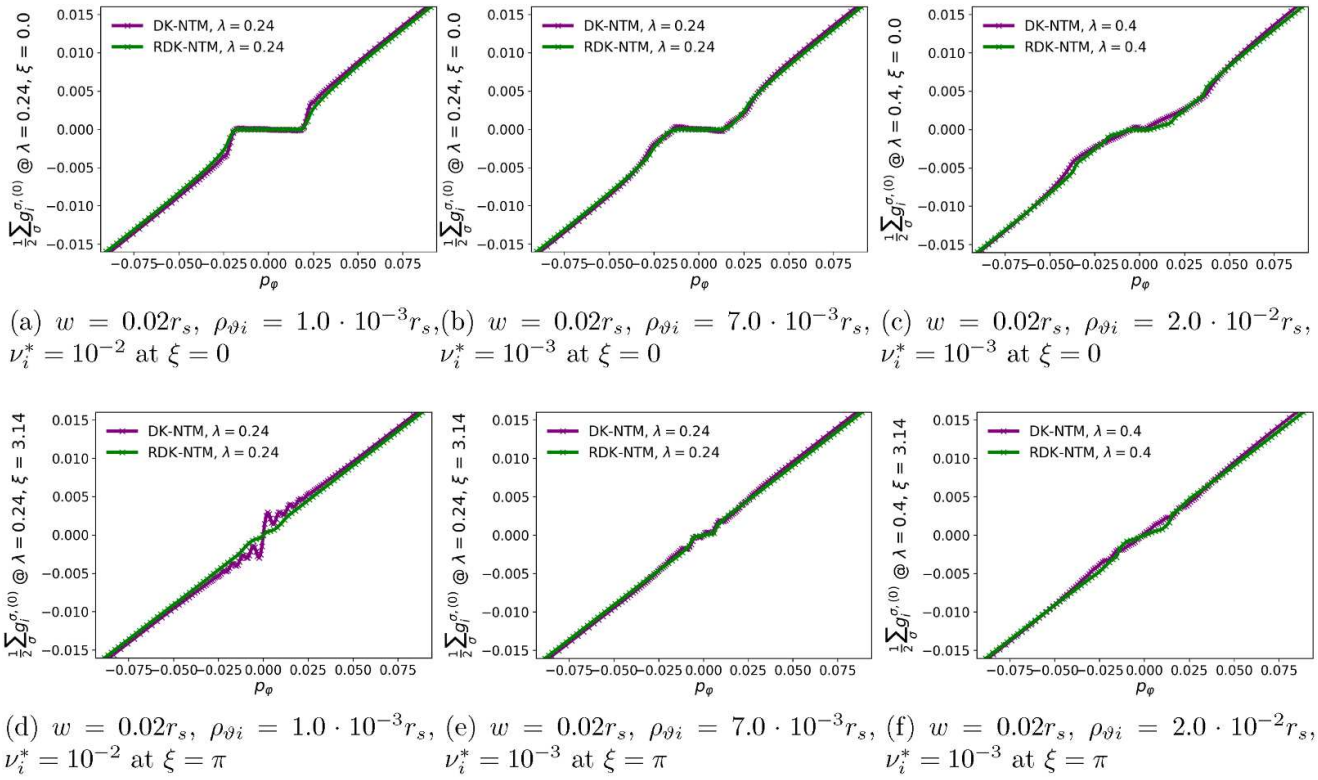

(a) $w = 0.02r_s$, $\rho_{\vartheta i} = 1.0 \cdot 10^{-3} r_s$, $\nu_i^* = 10^{-2}$ at $\xi = 0$

(b) $w = 0.02r_s$, $\rho_{\vartheta i} = 7.0 \cdot 10^{-3} r_s$, $\nu_i^* = 10^{-3}$ at $\xi = 0$

(c) $w = 0.02r_s$, $\rho_{\vartheta i} = 2.0 \cdot 10^{-2} r_s$, $\nu_i^* = 10^{-3}$ at $\xi = 0$

(d) $w = 0.02r_s$, $\rho_{\vartheta i} = 1.0 \cdot 10^{-3} r_s$, $\nu_i^* = 10^{-2}$ at $\xi = \pi$

(e) $w = 0.02r_s$, $\rho_{\vartheta i} = 7.0 \cdot 10^{-3} r_s$, $\nu_i^* = 10^{-3}$ at $\xi = \pi$

(f) $w = 0.02r_s$, $\rho_{\vartheta i} = 2.0 \cdot 10^{-2} r_s$, $\nu_i^* = 10^{-3}$ at $\xi = \pi$

Figure C2. The ion density moments, comparing the results of (R)DK-NTM models, plotted as a function of p_φ in the absence of Φ for different $\rho_{\vartheta i}$ close to the deeply passing limit for $\xi = 0$ (O-point) and $\xi = \pi$ (X-point). $w = 0.02r_s$, $\varepsilon = 0.1$, $\lambda_c = 0.91$, $\hat{L}_q = 1$, $L_B^{-1} = 0$, $L_n/L_{Ti} = 1$.

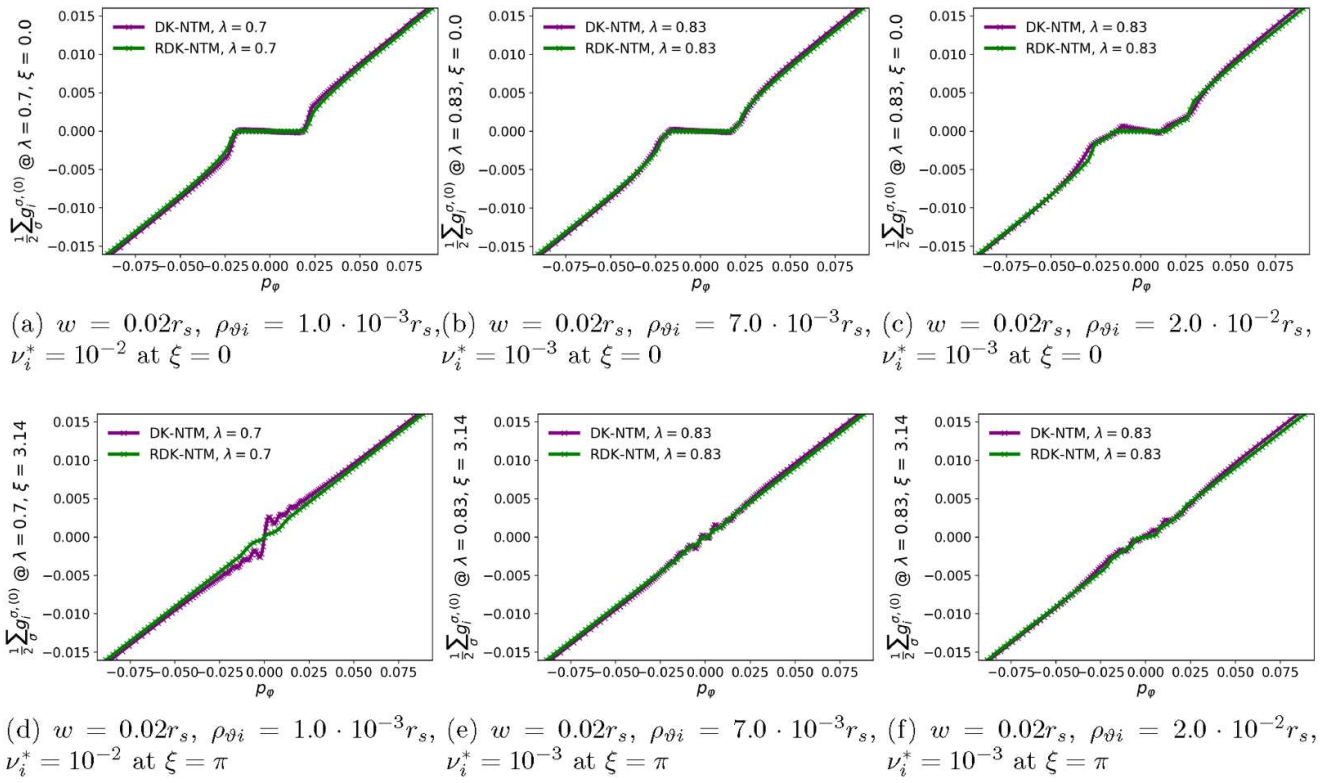

(a) $w = 0.02r_s$, $\rho_{\vartheta i} = 1.0 \cdot 10^{-3} r_s$, $\nu_i^* = 10^{-2}$ at $\xi = 0$

(b) $w = 0.02r_s$, $\rho_{\vartheta i} = 7.0 \cdot 10^{-3} r_s$, $\nu_i^* = 10^{-3}$ at $\xi = 0$

(c) $w = 0.02r_s$, $\rho_{\vartheta i} = 2.0 \cdot 10^{-2} r_s$, $\nu_i^* = 10^{-3}$ at $\xi = 0$

(d) $w = 0.02r_s$, $\rho_{\vartheta i} = 1.0 \cdot 10^{-3} r_s$, $\nu_i^* = 10^{-2}$ at $\xi = \pi$

(e) $w = 0.02r_s$, $\rho_{\vartheta i} = 7.0 \cdot 10^{-3} r_s$, $\nu_i^* = 10^{-3}$ at $\xi = \pi$

(f) $w = 0.02r_s$, $\rho_{\vartheta i} = 2.0 \cdot 10^{-2} r_s$, $\nu_i^* = 10^{-3}$ at $\xi = \pi$

Figure C3. Same as Figure C2, except that λ is close to the trapped-passing boundary, $\lambda_c = 0.91$.

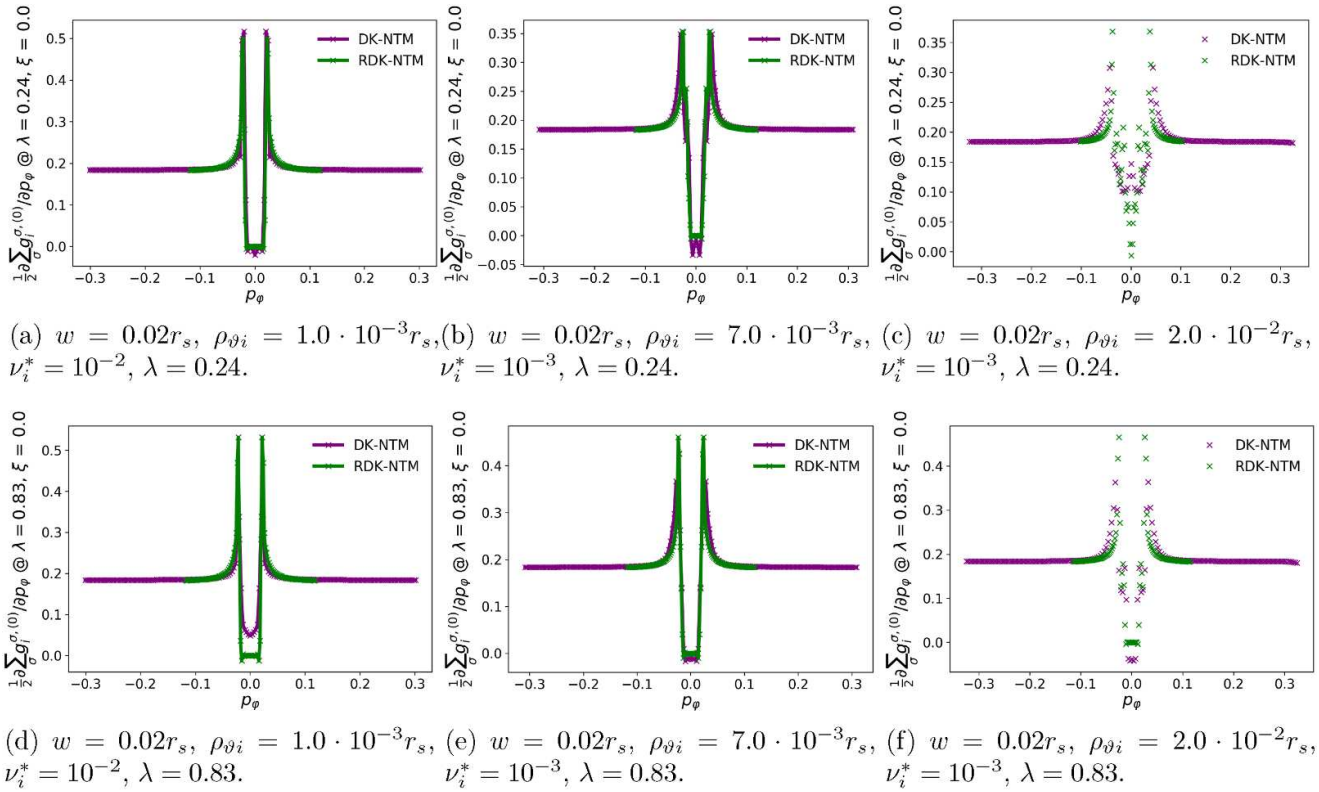

(a) $w = 0.02r_s$, $\rho_{\vartheta i} = 1.0 \cdot 10^{-3} r_s$, $\nu_i^* = 10^{-2}$, $\lambda = 0.24$.
(b) $w = 0.02r_s$, $\rho_{\vartheta i} = 7.0 \cdot 10^{-3} r_s$, $\nu_i^* = 10^{-3}$, $\lambda = 0.24$.
(c) $w = 0.02r_s$, $\rho_{\vartheta i} = 2.0 \cdot 10^{-2} r_s$, $\nu_i^* = 10^{-3}$, $\lambda = 0.24$.

(d) $w = 0.02r_s$, $\rho_{\vartheta i} = 1.0 \cdot 10^{-3} r_s$, $\nu_i^* = 10^{-2}$, $\lambda = 0.83$.
(e) $w = 0.02r_s$, $\rho_{\vartheta i} = 7.0 \cdot 10^{-3} r_s$, $\nu_i^* = 10^{-3}$, $\lambda = 0.83$.
(f) $w = 0.02r_s$, $\rho_{\vartheta i} = 2.0 \cdot 10^{-2} r_s$, $\nu_i^* = 10^{-3}$, $\lambda = 0.83$.

Figure C4. The ion density moments differentiated with respect to p_φ at fixed λ and ξ and plotted as a function of p_φ at the O-point at different λ in the absence of Φ. $w = 0.02r_s$, $\varepsilon = 0.1$, $\hat{L}_q = 1$, $L_B^{-1} = 0$, $L_n/L_{Tj} = 1$.

by the DK-NTM model; this is assumed to be numerical, but will be explored further in future. Since it is the density/temperature gradient that is responsible for the perturbation in the bootstrap current, in figure C4 we show the density moments, differentiated with respect to p_φ and plotted against p_φ to magnify any differences. The largest discrepancies are at the largest $\rho_{\vartheta i}/w$. We note from these comparisons that the (R)DK-NTM distribution functions agree reasonably well even around the S island separatrix, where the $\partial^2/\partial S^2$ term from the collision operator competes with the parallel streaming.

In figures C2–C4 we confirm that the impact of the drift islands on the density gradient inside the magnetic island increases with $\rho_{\vartheta i}$ as the radial shift of drift islands relative to the magnetic island becomes larger. At the same time, the effect of the radial shift seems to become less crucial as λ approaches the collisional dissipation layer, e.g. the ion density moment has a partially flat region across the island at $\lambda = 0.83$ even at a relatively large $\rho_{\vartheta i}/w = 0.35$ or 1. This might be explained by the fact that the passing solution close to $\lambda = \lambda_c$ is influenced by the trapped branch via the matching in the dissipation layer and vice versa: drift islands do not exist in the trapped region, but the magnetic island is still present and provides the flat solution in the vicinity of the O-point. Nevertheless, since the fraction of trapped particles is small, their contribution to the total density is insufficient to enforce the conventional flat profile across the magnetic island at large $\rho_{\vartheta i} w^{-1}$.

In figure C5 we show the flow moments, $(1/2)\sum_\sigma \sigma g_i^{(0),\sigma}$, in ψ space. As mentioned above, since the trapped particle solution is independent of σ at fixed p_φ, their contribution to the parallel flow is small, as we can see from figure C5(a). Both the DK- and RDK-NTM solutions demonstrate agreement with the drift island concept described above in the vicinity of the magnetic island and match the equilibrium neoclassical flows far from the island. At small $\rho_{\vartheta i}$, e.g. $\rho_{\vartheta i}/w = 0.05$, the DK-NTM solution has oscillations in the flow as ξ approaches the X-point as shown in figures C6(c) and C7(b). This is potentially numerical, noting that the diffusion term in p_φ or S space scales with $\rho_{\vartheta i}$ and will become difficult for the 4D DK-NTM model to resolve at small $\rho_{\vartheta i}/w$. This is true even at a relatively large $\nu_i^* = 10^{-2}$, e.g. see figures C2(g) and C3(g). This also explains why the best matching results are obtained at $\rho_{\vartheta i} \lesssim w$, while achieving smaller $\rho_{\vartheta i}/w$ becomes increasingly challenging for the 4D DK-NTM code as the transport terms become smaller. A similar discrepancy is found in collisionality. Indeed, the pitch angle scattering outside the dissipative layer is small and is dominated by the free streaming. A lower ν_j^* will decrease the collision operator further, making it difficult for the DK-NTM to resolve the collisional terms. In contrast, the RDK-NTM model requires low collisionality for particles to follow the S streamlines and to implement matching through the collisional boundary layer. We find, $\nu_i^* \sim (10^{-3}, 10^{-4})$ provides a narrow window where the validity regions of both solutions overlap.

To investigate the basis for the threshold, in figures C7(a), (b) and C8(a), (b) we integrate the flow moments over velocity space to provide the ion flow for both the DK- and RDK-NTM models for small and large $\rho_{\vartheta i}$. At $\rho_{\vartheta i}/w = 0.05$ (figures C7(a) and (b)), both the DK- and RDK-NTM reproduce the results of the conventional model for large magnetic islands with a zero flow profile across the island O-point and matching the neoclassical equilibrium far from the magnetic island. As discussed above, the flat region within the magnetic island decreases with increasing $\rho_{\vartheta i}/w$, as can be seen by comparing Figures 4, C8(a) and (b). At the same time, the peak region of the parallel flow right outside the separatrix becomes wider and is compensated by the contribution to the parallel flow that originated inside the island. As we can see from figures C8(a) and (b), this balancing contribution is mainly localised within the island region according to the DK-NTM predictions (blue area inside the island in figure C8(b)), while in the RDK-NTM solution it is concentrated around the X-point (blue areas closer to the X-point in figure C8(a)).

The origin of the negative DK-NTM flow in figure C8(b) inside the magnetic island is shown in figure C10. In contrast to the RDK-NTM solution, where $\sigma = \pm 1$ drift islands are located at the same level with the magnetic island, in accordance with equation (21), the DK-NTM distribution functions (and hence drift islands) for $\sigma = \pm 1$, along with the radial shift, are also vertically shifted relative to each other and to the magnetic island. The vertical shift of the distribution function is denoted by g_0 in figure C10. As we see from figures C10(b)–(d), DK-NTM predicts that g_0 is not constant but is a function of λ at fixed p_φ and/or ψ. At fixed p_φ and λ, the vertical shift is a function of ξ as well. Its origin in DK-NTM is to be investigated further as part of the future work. Note, as the DK-NTM solutions are vertically shifted by the same value, this vertical shift does not influence the density moments and thus they agree with the RDK-NTM solutions.

Now let us compare the (R)DK-NTM solution against the analytic solution found in [18]. The curvature of the distribution function in the vicinity of the island separatrix is determined by the diffusion terms that arise from transforming from ψ to S/p_φ in the pitch angle scattering collision operator. These transport terms are proportional to $\partial^k/\partial S^k\big|_{\lambda,\xi}$ or $\partial^k/\partial p_\varphi^k\big|_{\lambda,\xi}$ ($k = 1, 2$), respectively. In figure C9(c) we plot the leading order ion distribution function, differentiated with respect to y, against y, obtained with the full collision operator. For RDK-NTM this is the collision operator presented in appendix B. In figure C9(d) we plot the analytic result of [18] valid in the limit of large w ($\rho_{\vartheta i}/w = 0.05$ is chosen). This is to be denoted by $H96$. $H96$ is derived from a model diffusion of the form $\Gamma_\psi = -D\partial n/\partial\psi$, where Γ_ψ is the particle flux in the radial direction and D is the diffusion coefficient that has been assumed to be a slowly varying function across the magnetic island O-point. In figure C9(d) we also show the test RDK-NTM solution with the model radial diffusion weighted by $\sqrt{S + \cos\xi}$ (green markers)[12]. The latter reproduces well the $H96$ solution at large w outside the island. Figures C9(c) and (d) show that keeping the actual S diffusion is important; otherwise, a

[12] This is equivalent to diffusion taken in [18] in the limit of small $\rho_{\vartheta i}/w$.

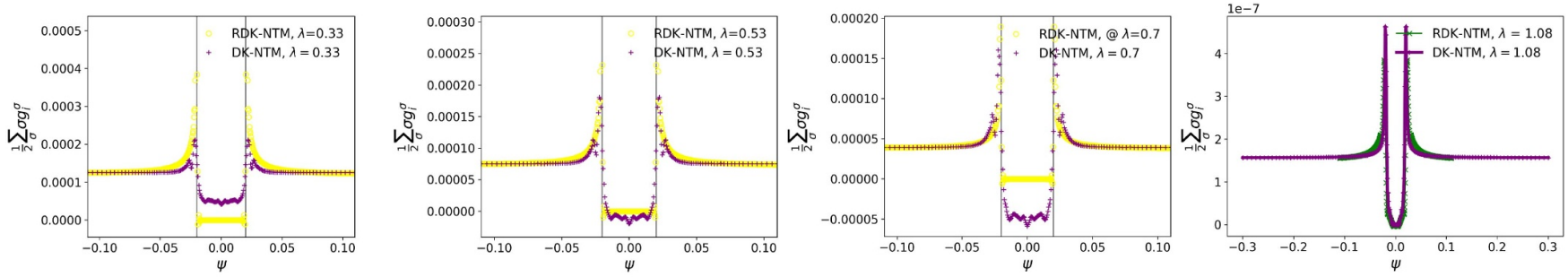

(a) $\xi = 0,\ \lambda = 0.33$ (b) $\xi = 0,\ \lambda = 0.53$ (c) $\xi = 0,\ \lambda = 0.70$ (d) $\xi = 0,\ \lambda = 1.08$

Figure C5. The ion flow moments plotted as a function of ψ across the O-point at different λ in the absence of Φ. The trapped-passing boundary is at $\lambda_c = 0.91$, $w = 0.02 r_s$, $\rho_{\vartheta i} = 1.0 \times 10^{-3} r_s$, $\nu_i^* = 10^{-4}$, $\varepsilon = 0.1$, $\hat{L}_q = 1$, $L_B^{-1} = 0$, $L_n/L_{Ti} = 1$.

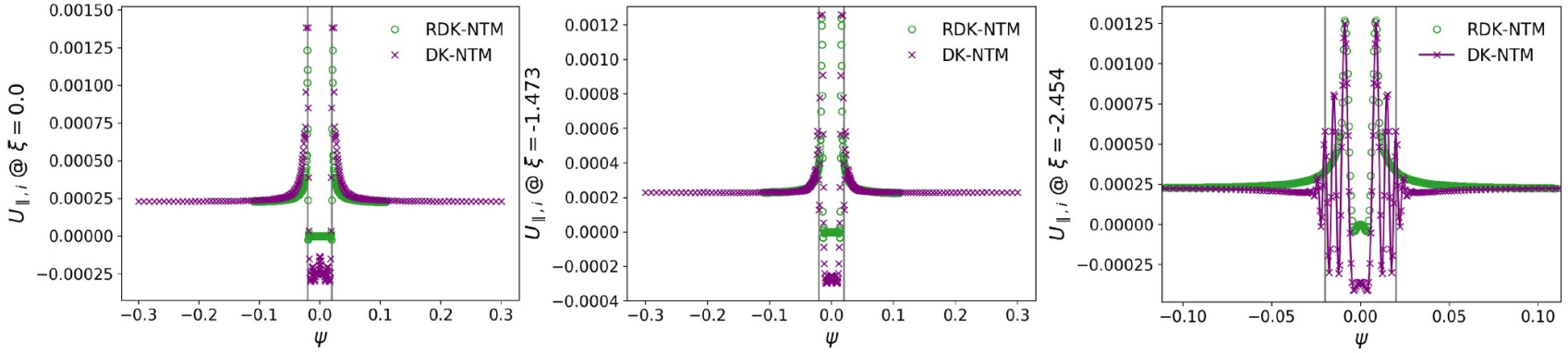

(a) $\xi = 0.$ (b) $\xi = -1.47$ (c) $\xi = -2.54$

Figure C6. The (R)DK-NTM ion parallel flow, $u_{\parallel i}$, radial profile at different ξ at $w = 0.02 r_s$, $\rho_{\vartheta i} = 1.0 \times 10^{-3} r_s$, $\nu_i^* = 10^{-3}$, $\varepsilon = 0.1$, $\hat{L}_q = 1$, $L_B^{-1} = 0$, $L_n/L_{Ti} = 1$. $u_{\parallel i}$ is normalised to V_{Ti}. The grey vertical lines indicate the position of the magnetic island separatrix.

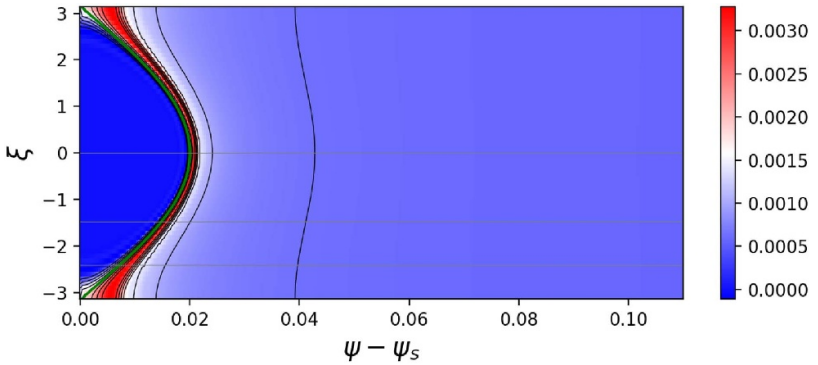

(a) The RDK-NTM ion flow contour in the (ψ, ξ) plane.

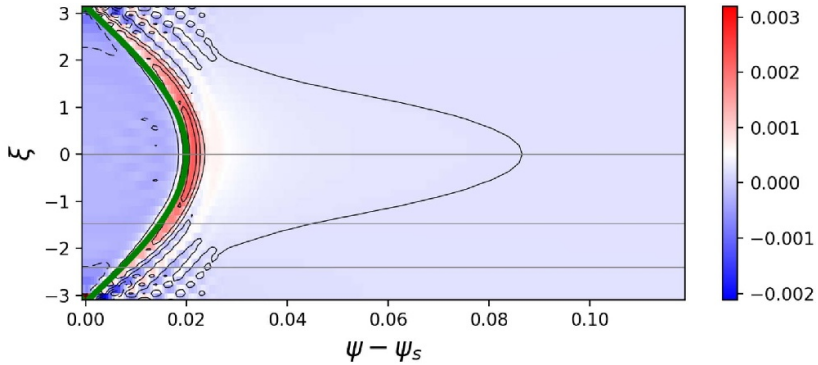

(b) The DK-NTM ion flow contour in the (ψ, ξ) plane.

Figure C7. The 2D contours of the ion parallel flow, corresponding to figures C6(a)–C6(c) for the RDK-NTM (a) and DK-NTM (b) models. The green line indicates the position of the magnetic island separatrix. The grey horizontal lines indicate the ξ values chosen in figures C6(a)–C6(c).

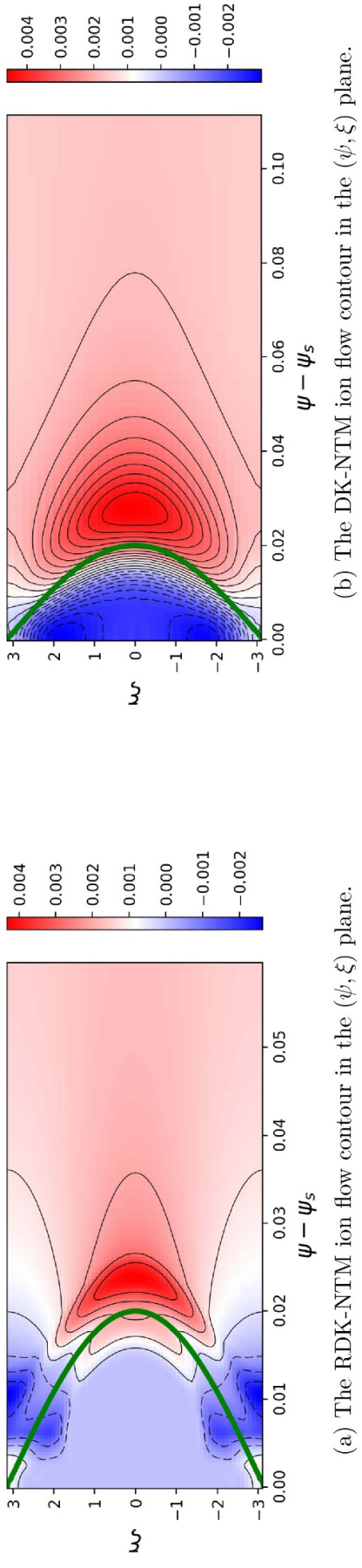

(a) The RDK-NTM ion flow contour in the (ψ, ξ) plane.

(b) The DK-NTM ion flow contour in the (ψ, ξ) plane.

Figure C8. The same as figures C7(a) and (b) except for $\rho_{\vartheta i} = 7.0 \times 10^{-3} r_s$.

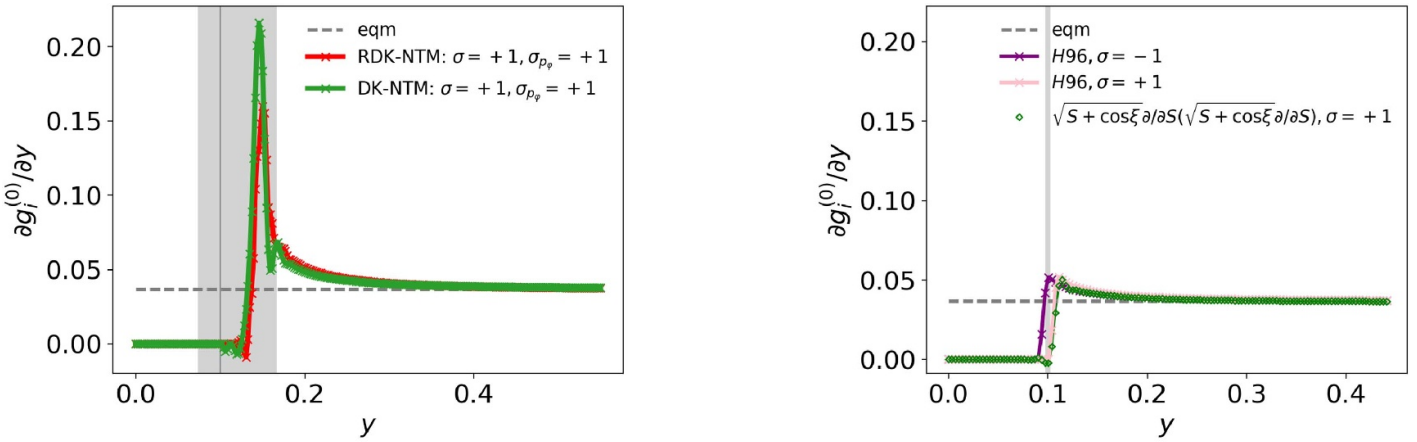

(a) The full (R)DK-NTM solution.

(b) The solution with the model radial diffusion.

Figure C9. The leading order ion distribution function, differentiated with respect to y, in the absence of the electrostatic potential plotted as a function of y at $\rho_{\vartheta i}/w = 0.05$. The grey dashed line shows the equilibrium gradient level in the absence of the magnetic island. The vertical grey line indicates the position of the S island separatrix. The grey area in (a) represents the boundary layer around the drift island separatrix. (a) Results from our two numerical models, employing collisional diffusion. (b) Analytic result from [18] for a model diffusion operator, labelled $H96$, compared to numerical results from RDK-NTM with a similar model diffusion replacing the collisional diffusion (green markers).

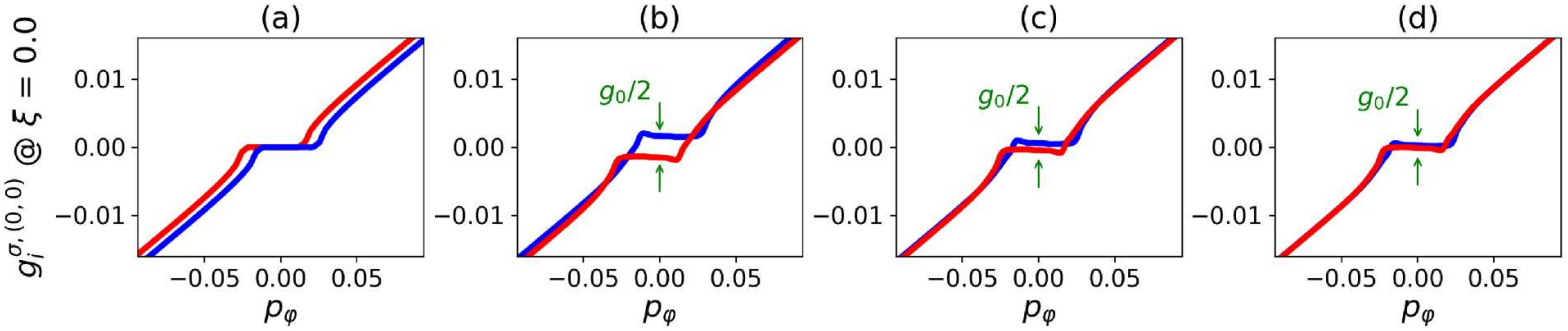

Figure C10. The RDK- (a) and DK-NTM (b)–(d) distribution functions plotted against p_φ for large $\rho_{\vartheta i}/w$. The blue/red distribution functions correspond to the $\sigma = +1/-1$ drift islands. The magnetic island is located between them. (a), (b) $\lambda = 0.24$, (c) $\lambda = 0.61$, (d) $\lambda = 0.83$.

significant fraction of the perturbation will be removed right outside the separatrix. A consequence of this is that our quantitative results may be sensitive to turbulent diffusion—a possibility to explore in the future.

A potential source of discrepancy between the DK- and RDK-NTM models is associated with a narrow boundary layer around the drift island separatrix. While the DK- and RDK-NTM $g_i^{(0)}$ seem to agree well in the vicinity of the separatrix, figure C9(c). shows that there is some difference in their y derivatives. In the vicinity of the drift island separatrix, there is a region where S derivatives drive a large diffusion which can be comparable to parallel streaming, $\nu_{ii/e}\partial^2/\partial S^2 \sim \mathcal{A}\partial/\partial\xi|_S$. This would invalidate the perturbative treatment of collisions in the RDK-NTM solver. This region is then to be treated in a way similar to the dissipative layer solution in λ space discussed above. This separatrix layer has been addressed to some extent in [21, 22, 29, 30], but without a complete treatment in toroidal geometry. Future extensions of the RDK-NTM model will address this, but it is not expected to influence the calculation of the bootstrap current and thus the result for the RDK-NTM magnetic island threshold presented in section 6. However, the difference shown in figure C9(c) might be crucial in calculating the polarisation current, which at this stage remains part of our future work (noting that here we consider stationary islands in the plasma $\boldsymbol{E}\times\boldsymbol{B}$ rest frame, for which the polarisation current is not expected to be important).

ORCID iDs

A V Dudkovskaia https://orcid.org/0000-0001-6890-3079
J W Connor https://orcid.org/0000-0001-9666-6103
D Dickinson https://orcid.org/0000-0002-0868-211X
P Hill https://orcid.org/0000-0003-3092-1858
S Leigh https://orcid.org/0000-0002-0376-9451
H R Wilson https://orcid.org/0000-0003-3333-7470

References

[1] Qu W X and Callen J D 1985 *University of Wisconsin Report* UWPR 85-5
[2] Carrera R, Hazeltine R D and Kotschenreuther M 1986 *Phys. Fluids* **29** 899
[3] Furth H P, Killeen J and Rosenbluth M N 1963 *Phys. Fluids* **6** 459
[4] Dominguez R R and Waltz R E 1987 *Nucl. Fusion* **27** 65
[5] Snipes J A *et al* 1990 *Nucl. Fusion* **30** 205
[6] Hender T C *et al* 2007 *Nucl. Fusion* **47** S128–202
[7] Sauter O *et al* 1997 *Phys. Plasmas* **4** 1654
[8] Sauter O *et al* 2002 *Plasma Phys. Control. Fusion* **44** 1999–2019
[9] Buttery R J *et al* 2000 *Plasma Phys. Control. Fusion* **42** B61–73
[10] Strauss H R 2004 *Phys. Fluids* **24** 1981
[11] Hegna C C and Callen J D 1994 *Phys. Plasmas* **1** 2308
[12] Chang Z, Fredrickson E D and Batha S H 1998 *Phys. Plasmas* **5** 1076
[13] Rutherford P H 1973 *Phys. Fluids* **16** 1903–8
[14] Glasser A H, Greene J M and Johnson J L 1975 *Phys. Fluids* **18** 875
[15] Lutjens H, Luciani J-F and Garbet X 2001 *Phys. Plasmas Lett.* **8** 4267–70
[16] Connor J W, Waelbroeck F L and Wilson H R 2001 *Phys. Plasmas* **8** 2835
[17] Fitzpatrick R, Waelbroeck F L and Militello F 2006 *Phys. Plasmas* **13** 122507
[18] Wilson H R, Connor J W, Hastie R J and Hegna C C 1996 *Phys. Plasmas* **3** 248
[19] Chang Z *et al* 1995 *Phys. Rev. Lett.* **74** 4663–6
[20] Gibson K J *et al* 2010 *Plasma Phys. Control. Fusion* **52** 124041
[21] Fitzpatrick R 1995 *Phys. Plasmas* **2** 825
[22] Hazeltine R D, Helander P and Catto P J 1997 *Phys. Plasmas* **4** 2920
[23] Smolyakov A I 1993 *Plasma Phys. Control. Fusion* **35** 657
[24] Wilson H R *et al* 1996 *Plasma Phys. Control. Fusion* **38** A149
[25] Kuvshinov B N and Mikhailovskii A B 1998 *Plasma Phys. Rep.* **24** 245–68
Kuvshinov B N and Mikhailovskii A B 1998 Translated from Fizika Plasmy *Fiz. Plasmy* **24** 275–92
[26] Mikhailovskii A B, Pustovitov V D and Smolyakov A I 2000 *Plasma Phys. Control. Fusion* **42** 309
[27] Waelbroeck F L, Connor J W and Wilson H R 2001 *Phys. Rev. Lett.* **87** 215003–1
[28] Bergman A, Poli E and Peeters A G 2005 *Phys. Plasmas* **12** 072501
[29] James M and Wilson H R 1647–59 *Plasma Phys. Control. Fusion* **48** 2006
[30] James M, Wilson H R and Connor J W 2010 *Plasma Phys. Control. Fusion* **52** 075008
[31] Buttery R J *et al* 2002 *Phys. Rev. Lett.* **88** 125005–1
[32] La Haye R J *et al* 2006 *Nucl. Fusion* **46** 451–61
[33] La Haye R J *et al* 2012 *Phys. Plasmas* **19** 062506
[34] Imada K *et al* 2018 *Phys. Rev. Lett.* **121** 175001
[35] Imada K *et al* 2018 *J. Phys.: Conf. Ser.* **1125** 012013
[36] Imada K *et al* 2019 *Nucl. Fusion* **59** 046016
[37] Poli E *et al* 2002 *Phys. Rev. Lett.* **88** 075001
[38] Poli E *et al* 2003 *Plasma Phys. Control. Fusion* **45** 71–87
[39] Dudkovskaia A 2019 Modelling neoclassical tearing modes in tokamak plasmas *PhD Thesis* University of York
[40] Kadomtsev B B 1991 *Nucl. Fusion* **31** 1301
[41] Dudkovskaia A V, Garbet X, Lesur M and Wilson H R 2019 *Nucl. Fusion* **59** 086010
[42] Imada K, Connor J W, Dudkovskaia A V, Hill P and Wilson H R 2019 Benchmarking of the Drift Kinetic Model for the NTM Threshold *46th EPS Conference on Plasma Physics* (Milan)